

A Spatial Gap in the Sky Distribution of Fast Radio Burst Detections Coinciding with Galactic Plasma Overdensities

SWARALI SHIVRAJ PATIL,^{1,2} ROBERT A. MAIN,^{3,4} EMMANUEL FONSECA,^{1,2} KYLE MCGREGOR,^{3,4} B. M. GAENSLER,^{5,6,7}
CHARANJOT BRAR,⁸ AMANDA M. COOK,^{3,4,9} ALICE P. CURTIN,^{3,4} GWENDOLYN EADIE,^{7,10} RONNIY JOSEPH,^{3,4}
LORDRICK KAHINGA,^{5,11} VICTORIA KASPI,^{3,4} AFROKK KHAN,^{3,4} BIKASH KHAREL,^{1,2} ADAM E. LANMAN,^{12,13} CALVIN LEUNG,^{14,15}
KIYOSHI W. MASUI,^{12,13} MASON NG,^{3,4} KENZIE NIMMO,¹² AYUSH PANDHI,^{7,6} AARON B. PEARLMAN,^{3,4} ZIGGY PLEUNIS,^{9,16}
MAWSON W. SAMMONS,^{3,4} KETAN R. SAND,^{3,4} PAUL SCHOLZ,^{17,6} KAITLYN SHIN,^{12,13} SETH R. SIEGEL,^{18,3,4} AND
KENDRICK SMITH¹⁸

¹Department of Physics and Astronomy, West Virginia University, PO Box 6315, Morgantown, WV 26506, USA

²Center for Gravitational Waves and Cosmology, West Virginia University, Chestnut Ridge Research Building, Morgantown, WV 26505, USA

³Department of Physics, McGill University, 3600 rue University, Montréal, QC H3A 2T8, Canada

⁴Trottier Space Institute, McGill University, 3550 rue University, Montréal, QC H3A 2A7, Canada

⁵Department of Astronomy and Astrophysics, University of California, Santa Cruz, 1156 High Street, Santa Cruz, CA 95064, USA

⁶Dunlap Institute for Astronomy and Astrophysics, 50 St. George Street, University of Toronto, ON M5S 3H4, Canada

⁷David A. Dunlap Department of Astronomy and Astrophysics, 50 St. George Street, University of Toronto, ON M5S 3H4, Canada

⁸NRC Herzberg Astronomy and Astrophysics, 5071 West Saanich Road, Victoria, BC V9E2E7, Canada

⁹Anton Pannekoek Institute for Astronomy, University of Amsterdam, Science Park 904, 1098 XH Amsterdam, The Netherlands

¹⁰Department of Statistical Science, University of Toronto, Ontario Power Building, 700 University Avenue, 9th Floor, Toronto, ON M5G 1Z5, Toronto, Ontario, Canada

¹¹Department of Physics, College of Natural and Mathematical Sciences, University of Dodoma, 1 Benjamin Mkapa Road, 41218 Iyumbu, Dodoma 259, Tanzania

¹²MIT Kavli Institute for Astrophysics and Space Research, Massachusetts Institute of Technology, 77 Massachusetts Ave, Cambridge, MA 02139, USA

¹³Department of Physics, Massachusetts Institute of Technology, 77 Massachusetts Ave, Cambridge, MA 02139, USA

¹⁴Miller Institute for Basic Research, University of California, Berkeley, CA 94720, United States

¹⁵Department of Astronomy, University of California, Berkeley, CA 94720, United States

¹⁶ASTRON, Netherlands Institute for Radio Astronomy, Oude Hoogeveensdijk 4, 7991 PD Dwingeloo, The Netherlands

¹⁷Department of Physics and Astronomy, York University, 4700 Keele Street, Toronto, ON M3J 1P3, Canada

¹⁸Perimeter Institute of Theoretical Physics, 31 Caroline Street North, Waterloo, ON N2L 2Y5, Canada

ABSTRACT

We analyze the positional and morphological properties of about 3600 unique fast radio burst (FRB) sources reported in the second FRB catalog generated by the Canadian Hydrogen Intensity Mapping Experiment (CHIME) telescope. We find a two-dimensional dependence of FRB detections on sky position, and identify a significant absence of detections in a roughly circular region centered at Galactic coordinates $(77.7^\circ, 0.9^\circ)$, spanning an area of 216.2 deg^2 . This detection gap spatially coincides with the Cygnus X region – a plasma-rich star-forming region in the Milky Way. This lack of FRB detections is most likely the result of increased sky temperature and strong multi-path scattering by turbulent ionized plasma, which broadens the FRB signals beyond detectability in the CHIME band. Our simulations yield a mean of 6 expected FRB detections within the gap when accounting for the elevated sky temperature in the direction of the detection gap. We infer that a lower limit of the maximum scattering timescale $\tau_{\text{sc}, 1\text{GHz}} \geq 4.13 \text{ ms}$ is sufficient to suppress the observed signal-to-noise ratio of all FRBs. In addition to Cygnus X, a similar suppression is seen in Catalog 2 along other high-emission measure (EM) sightlines (i.e., $\text{EM} \geq 2900 \text{ pc cm}^{-6}$), further supporting a broader trend of suppression due to Galactic scattering. Future very long baseline interferometry (VLBI) measurements of scattering disks with CHIME Outriggers could help confirm our interpretation. Our work highlights the substantial impact of the ionized and turbulent Galactic interstellar medium on the detectability of FRBs.

Corresponding author: Swarali Shivraj Patil

sp00049@mix.wvu.edu

Keywords: Radio bursts (1339) — Radio transient sources (2008) — Interstellar scattering (854) — Interstellar plasma (851) — High energy astrophysics (739)

1. INTRODUCTION

Fast radio bursts (FRBs) are bright and brief extragalactic bursts of energy emitted in the radio spectrum (D. R. Lorimer et al. 2007, also see E. Petroff et al. 2022 for a recent overview). While their origins remain unclear, there are a growing number of observations that support models based on compact objects, such as highly magnetized neutron stars (e.g. CHIME/FRB Collaboration et al. 2020; C. D. Bochenek et al. 2020, see E. Platts et al. 2019 for a collection of proposed models). Regardless of their origins, FRBs undergo the same dispersive and scatter-broadening effects regularly observed in Galactic radio pulsars (S. K. Ocker et al. 2022), with scattering arising from dense ionized regions in near-source environments within their host galaxies and/or the Milky Way. Scattering often needs to be modeled with one or more distinct scattering screens – a framework developed for pulsars (I. P. Williamson 1972) and subsequently applied to FRBs. In this sense, FRBs can be used as powerful probes of the electron density fluctuations in the interstellar medium (ISM) along their lines of sight.

Along a given line of sight (LOS), the scattering timescale (τ_{sc}) characterizes the time delay caused by multi-path propagation through the warm ionized medium (WIM). Propagation through ionized plasma also results in a frequency-dependent dispersive delay that is proportional to the integrated column density of free electrons along the LOS. This integrated quantity is known as the dispersion measure (DM). Based on the DM and τ_{sc} predictions from the NE2001 Galactic electron density model (J. M. Cordes & T. J. W. Lazio 2002), S. K. Ocker et al. (2022) postulated a “zone of avoidance” to span over a range of Galactic longitudes $|l| \leq 50^\circ$ and latitudes $|b| \leq 4.1^\circ$ at 0.4 GHz for FRBs. J.-P. Macquart & S. Johnston (2015) proposed that diffractive scintillation enhances FRB detectability at higher Galactic latitudes by boosting some bursts above the detection threshold, particularly in the presence of a steep luminosity distribution. Strong scattering in the Galactic plane can suppress scintillation and broaden the pulse, reducing the likelihood of such boosts.

Studies of the FRB sky distribution have been limited by the small number of detections and the challenges associated with combining data from different instruments, each with differing sensitivities, instrumental uncertainties, and selection functions. The FRB sky distribution can greatly vary based on the observing frequency. As a result, the scope of such studies so far has been limited to probing only the Galactic latitude dependence. Using data acquired with the Canadian Hydrogen Intensity Mapping Experiment

(CHIME) Fast Radio Burst project (hereafter, CHIME/FRB), A. Joseph et al. (2021) reported no significant dependence of FRB detections on Galactic latitude in CHIME/FRB Catalog 1 (CHIME/FRB Collaboration et al. 2021) containing 536 FRBs.

The forthcoming second catalog of CHIME/FRB (hereafter Catalog 2) represents a significant advancement, reporting the largest number of unique FRBs detected by a single instrument (CHIME/FRB Collaboration et al. 2025). An updated map of the FRB sky positions in Catalog 2 reveals a striking and visually discernible gap in FRB detections. For the first time, we clearly identify a Galactic scattering zone of avoidance (hereafter referred to as the “detection gap”) in FRB detections, which spans Galactic longitudes $70^\circ < l < 90^\circ$ and latitudes $-7^\circ < b < 11^\circ$ in the CHIME observing band (400–800 MHz). This detection gap coincides with the Cygnus X region – a massive star-forming region in the Galaxy, known to contain dense ionized gas and strong degrees of turbulence (J. H. Piddington & H. C. Minnett 1952a; H. J. Wendker et al. 1991; N. Schneider et al. 2006). The alignment with known Galactic structure suggests a strong link between plasma propagation effects and the suppression of FRB detectability in the CHIME/FRB experiment.

This study reports a detailed analysis of the detection gap, investigates the extent to which propagation effects contribute to it and identifies associated patterns in scattering and detectability. The structure of the paper is as follows. In §2, we describe the observational dataset including post-detection selection criteria and classification of FRBs based on morphology. In §3 we present evidence for a significant detection gap observed in the sky distribution of CHIME/FRB Catalog 2. In §4, we explore potential observational and astrophysical explanations for the detection gap, and derive an empirical lower bound on τ_{sc} responsible for it. The role of Galactic scattering in shaping FRB detectability across the full Catalog 2 sample is discussed in §5. Our conclusions are summarized in §6.

2. OBSERVATIONS

In this work, we analyze data products generated by the CHIME/FRB backend for Catalog 2 (CHIME/FRB Collaboration et al. 2025). Full descriptions of the CHIME telescope and its radio-transient backends are provided in other works (CHIME/FRB Collaboration et al. 2018; CHIME/Pulsar Collaboration et al. 2021; CHIME Collaboration et al. 2022). We nonetheless summarize aspects of CHIME and the Catalog 2 data products relevant to our study in this section.

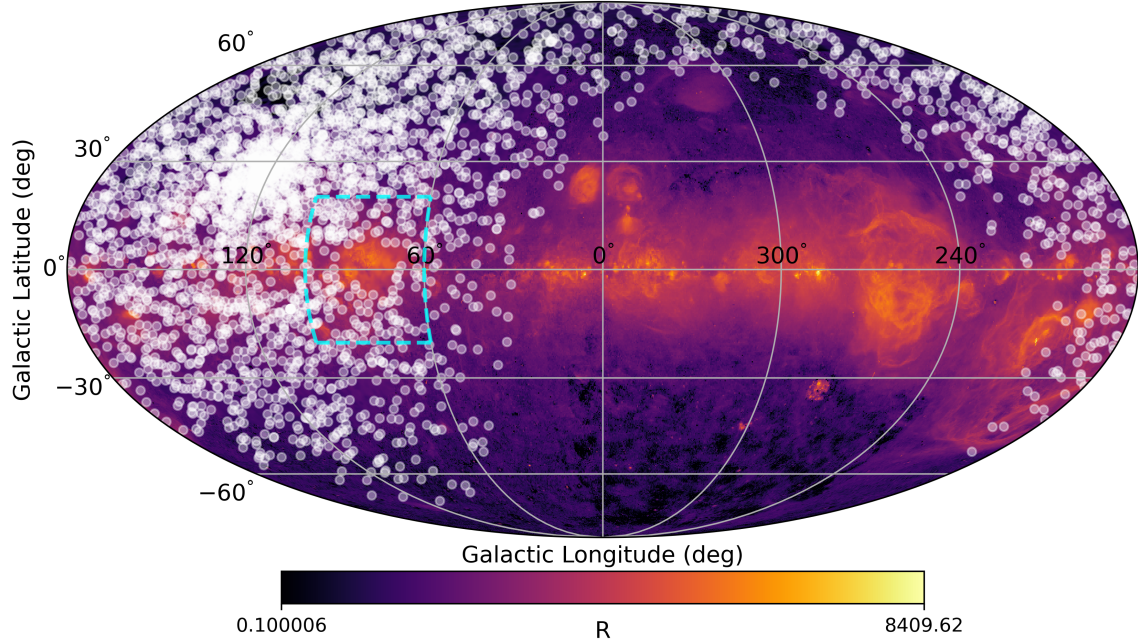


Figure 1. Positions of 3552 FRBs in our sample overlaid with the [D. P. Finkbeiner \(2003\)](#) $H\alpha$ intensity map in units of Rayleighs (R), where $1R = 10^6/4\pi \text{ photons cm}^{-2}\text{s}^{-1}\text{sr}^{-1}$. We qualitatively see an anti-correlation between FRB detections and the regions with overdensity of $H\alpha$. The detection gap is highlighted with dashed cyan lines. A zoomed-in view of this region is presented in Figure 2.

2.1. The CHIME Telescope and Instrumentation

The CHIME telescope is a compact radio interferometer that consists of 1,024 dual-polarization antennas operating in the 400–800 MHz range. These antennae are distributed across four half-cylindrical reflectors that collectively span $80\text{ m} \times 100\text{ m}$. The CHIME/FRB backend receives up to 1,024 streams of beamformed, total-intensity data with time and frequency resolutions of $t_{\text{samp}} \approx 0.983\text{ ms}$ and $\Delta\nu_{\text{chan}} \approx 24.4\text{ kHz}$, respectively ([CHIME/FRB Collaboration et al. 2018](#)), and enacts a series of real-time pipelines to identify and preserve astrophysical signals for further analysis. The CHIME/FRB detection pipeline uses a cut-off of signal-to-noise ratio – $(S/N) \geq (S/N)_{\text{thresh}} = 8$ – for filtering FRB candidates ([CHIME/FRB Collaboration et al. 2025](#)).

2.2. FRB Celestial Positions

The celestial position of each FRB is computed from total-intensity data using the procedure described by [CHIME/FRB Collaboration et al. \(2019\)](#). This procedure uses two pieces of information – the real-time metadata corresponding to the detecting beam, and an analytic model of the beam shape and FRB dynamic spectrum – to estimate a position and its statistical uncertainty. These localizations have typical uncertainties of $O(10')$. We caution that $O(1\%)$ of bright Catalog 2 FRBs may be incorrectly localized to the near-sidelobes, which can cause a position offset of 0.5° – 2° . This localization error does not have a significant impact on our analysis of the detection gap as the error magnitude is

much smaller than the angular extent of the gap. However, this could impact the classification of H II intersections described in §5.2. We encourage a follow-up of this work using more accurate localizations.

2.3. Model-dependent Classification of FRBs

Statistically significant signals detected by the CHIME/FRB backend are classified as “Galactic”, “ambiguous”, or “extragalactic”, based on the source position and DM estimated by the real-time *bonsai* tree de-dispersion algorithm ([CHIME/FRB Collaboration et al. 2018](#)). Single pulses from Galactic radio pulsars are identified through coincidences in both position and DM, and for the purposes of Catalog 2 are excluded from subsequent analysis. Our signals of interest are those deemed extragalactic (i.e., FRBs), which are classified as such if their DMs exceed both of the predicted maximum values from the NE2001 ([J. M. Cordes & T. J. W. Lazio 2002](#)) and YMW16 ([J. M. Yao et al. 2017](#)) electron density models for their lines of sight; these predictions are made assuming a distance of 25 kpc between the observer and the edge of the Milky Way disk. No aspects of scatter-broadening are considered for the real-time classification of FRBs.

2.4. Best-fit Models of FRB Morphology

In order to characterize the effects of the WIM on burst morphology in Catalog 2, we use spectro-temporal measurements of FRB morphology estimated with *fitburst* ([E. Fonseca et al. 2024](#)). The *fitburst* modeling framework

assumes that each pulsed feature undergoes cold-plasma dispersion and, in the absence of scattering-broadening, has a Gaussian shape of intrinsic temporal width (σ). If relevant, the shape of the burst is instead assumed to be the pulse broadening function of a Gaussian profile (e.g., [M. M. McKinnon 2014](#)) that depends on σ and τ_{sc} .

All Catalog 2 `fitburst` measurements assume that τ_{sc} scales with electromagnetic frequency (ν) such that $\tau_{\text{sc}} \propto \nu^{-4}$. The Catalog 2 values for τ_{sc} are originally reported referenced to $\nu = 400.195$ MHz ([CHIME/FRB Collaboration et al. 2025](#)); however, for this present study we scale τ_{sc} to be referenced at $\nu = 1$ GHz using $\tau_{\text{sc}, \nu} \propto \nu^{-4}$ ([N. D. R. Bhat et al. 2004](#)), as is typically done for related studies on radio pulsars and FRBs. Additionally, for detectability discussions, we reference τ_{sc} to CHIME frequencies whenever relevant – explicitly denoting it as $\tau_{\text{sc}, 600\text{MHz}}$. We used $\tau_{\text{sc}, 1\text{GHz}} > 0.13$ ms as a threshold for determining which FRBs have “well-measured” scatter-broadening; this threshold value was obtained through comparisons of `fitburst` fits between total-intensity and microsecond-resolution baseband (voltage) data of the same detections ([K. R. Sand et al. 2025](#)).

2.5. Post-detection Selection Criteria for Catalog 2 FRBs

We adopted the initial data quality flags outlined in the Catalog 2 methodology ([CHIME/FRB Collaboration et al. 2025](#)). In addition, we required that the event had successful fits from the `header_localization` and `fitburst` pipelines. We excluded FRBs detected in the sidelobes of the primary beam, since these are more complicated to localize accurately ([H.-H. Lin et al. 2024](#)). The above selection criteria resulted in 4439 FRBs. To obtain the full set of unique sightlines from Catalog 2, we retain only the burst with the highest (S/N) for each repeating source. The final sample utilized in this study consists of 3552 FRBs – comprising 3469 non-repeaters and 83 unique sightlines from repeating FRBs. Of those, 1146 FRBs meet the criterion for well-measured $\tau_{\text{sc}, 1\text{GHz}}$ described in §2.4.

3. A DETECTION GAP IN THE SKY DISTRIBUTION OF FRBS

Figure 1 presents the spatial distribution of FRBs in Catalog 2, with the detection gap region highlighted by a cyan dashed enclosure. The high density of FRB detections near the North Celestial Pole is due to CHIME’s declination-dependent sensitivity and exposure. A magnified view of the detection gap region is presented in Figure 2. To delineate its shape and extent, we applied geometric methods based on the Delaunay triangulation and its dual, the Voronoi diagram using the `scipy.spatial` module ([P. Virtanen et al. 2020](#)). Using the Voronoi diagram, we identified the largest empty circle within the detection gap by locating the Voronoi

vertices farthest from any FRB. We estimate the center of the largest empty circle (LEC) within the detection gap to be at $(l, b) = (77.7^\circ, 0.9^\circ)$, with a radius of $R_{\text{LEC}} = 7.7^\circ$. The triangulation partitions FRB positions into non-overlapping triangles such that no point is inside the circumcircle of any triangle. We identified the triangles for which the distance between their circumcenters and the center of gap fell within the radius. The convex hull obtained from connecting the outer boundary of these triangles is the polygon that encloses the sky with zero FRB detections in Figure 2, with an area of 216.2 deg^2 .

At 600 MHz, the effective gain of CHIME along the detection gap LOS is $G \approx 1.02$ K/Jy with system temperature $T_{\text{sys}} \approx 50$ K ([CHIME/FRB Collaboration et al. 2018](#)). Thus, the system equivalent flux density (SEFD) is roughly $T_{\text{sys}}/G \approx 48.78$ Jy. The single-pulse radiometer equation gives a minimum detectable flux density of ~ 0.5 Jy for narrow pulses (~ 1 ms broadened width) and ~ 0.1 Jy for pulses with broadened width larger than 10 ms along this LOS. In the following discussion, we assess whether the apparent detection gap can be explained by instrumental sensitivity and statistical noise effects, or whether it points to suppression in detectability due to scattering caused by ionized Galactic structures.

3.1. Statistical Significance of the Gap

To evaluate the significance of the lack of detections, we compute the probability of detecting 0 FRBs within a circle of radius R_{LEC} or larger anywhere on the sky surveyed by CHIME/FRB assuming a non-homogeneous Poisson process model for its detections. The non-homogeneous Poisson process is described by a position-dependent intensity function $\lambda(\alpha, \delta)$ which here represents the expected density of detected FRBs and scales with the instrument’s exposure and sensitivity. It is convenient to work in the equatorial coordinate system (α, δ) as the CHIME/FRB gain varies primarily with δ . Moreover, the cosine dependence of an isotropic universal distribution of FRBs on the celestial sphere cancels out with the inverse-cosine dependence of the exposure in declination.

As reported by [CHIME/FRB Collaboration et al. \(2021\)](#), we note reduced exposure between $27^\circ < \delta < 34^\circ$ as shown in Figure 8 in Appendix C and Figure 5 of [CHIME/FRB Collaboration et al. 2021](#). This is due to a time-limited failure of one of the four CPU nodes covering these declinations. The patch of reduced exposure overlaps with only 7% of the total sky area of the detection gap. Omitting the reduced exposure patch, we fit a polynomial to the logarithm of the exposure from Catalog 2 versus δ and find that the observed exposure in this region is $\approx 18\%$ lower than expected. At $\delta > 70^\circ$, sources are circumpolar from CHIME’s latitude and cross the telescope’s meridian twice daily. These ‘upper’ and ‘lower’

transits therefore yield higher effective exposure at $\delta > 70^\circ$. Using the CHIME/FRB sensitivity approximation parameterized by A. M. Cook et al. (2024) and accounting for exposure as described above, we can write

$$\lambda(\alpha, \delta) = \frac{1}{A} \left[(\cos^{1.5}(\phi - \delta))^{\gamma-1} + H(\delta - 70^\circ) (\cos^{1.5}(180^\circ - \phi - \delta))^{\gamma-1} \right] \quad (1)$$

where $H(x)$ is the Heaviside step function, $\gamma = 1.5$ is the Euclidean power-law index for a flux-limited survey representing the FRB luminosity function, $\phi = 49.32^\circ$ is the geographic latitude of the CHIME telescope (CHIME/FRB Collaboration et al. 2018), and A is the following normalization constant such that the intensity equals N_{total} , the total number of FRBs in the sample, when integrated over CHIME/FRB's sky:

$$A = \frac{2\pi}{N_{\text{total}}} \left[\int_{-11^\circ}^{90^\circ} (\cos^{1.5}(\phi - \delta))^{\gamma-1} d\delta + \int_{70^\circ}^{90^\circ} (\cos^{1.5}(180^\circ - \phi - \delta))^{\gamma-1} d\delta \right]. \quad (2)$$

The probability of detecting zero bursts within a circle of the observed radius R_{LEC} or larger anywhere on the sky can then be written as

$$P(N = 0 \in C(R_{\text{LEC}}) | \lambda) = \int_{0^\circ}^{360^\circ} \int_{-11^\circ}^{90^\circ} \exp \left[- \iint_{C(R_{\text{LEC}}, \{\alpha_0, \delta_0\})} \lambda(\alpha_0, \delta_0) d\alpha_0 d\delta_0 \right] \cos \delta d\alpha d\delta, \quad (3)$$

where $C(R_{\text{LEC}}, \{\alpha, \delta\})$ denotes the circle of radius R_{LEC} centered at $\{\alpha, \delta\}$. This probability serves as our one-sided p -value. We find that the non-detection of bursts in a region of this radius is statistically significant at the 4.2σ level obtained by converting $p \approx 1.3 \times 10^{-5}$ using the inverse survival function of the standard normal distribution.

3.2. Effect of the Sky Temperature

The spatial gap is towards Cygnus X (J. H. Piddington & H. C. Minnett 1952b), a bright source of radio continuum at CHIME's observing frequencies which could reduce sensitivity to a background burst. Using the Haslam 408 MHz radio sky temperature map (C. G. T. Haslam et al. 1982), scaled to the central frequency of the CHIME band with a scaling index of -2.6 , the average sky temperature within the detection gap is 35 K. To capture the effect of higher temperatures present in smaller sub-regions within the area, we use the 99th percentile $T_{\text{sky}} = 108$ K.

The expression for $(S/N)_b$, the signal-to-noise ratio of the broadened pulse,

$$(S/N)_b = \frac{GS_i \sqrt{n_p \Delta\nu}}{\beta(T_{\text{sys}} + T_{\text{sky}})} \frac{W_i}{\sqrt{W_b}} \quad (4)$$

follows directly from the standard radiometer equation as used in FRB and pulsar literature (e.g., J. M. Cordes & M. A. McLaughlin 2003; C. Patel et al. 2018), where S_i is the intrinsic flux density, n_p is the number of polarizations measured, $\Delta\nu$ is the bandwidth and β is the correction factor for digitization. Burst detectability for CHIME/FRB is governed by the intrinsic burst width W_i , intrinsic flux, DM and τ_{sc} . The observed peak flux density for an FRB decreases as its broadened pulse width - W_b - increases, defined as (D. W. Gardenier et al. 2021)

$$W_b = \sqrt{W_i^2(1+z_0)^2 + \tau_{\text{sc}}^2 + t_{\text{samp}}^2 + t_{\text{chan}}^2}, \quad (5)$$

where z_0 is the redshift and t_{chan} depends linearly on the DM as described by Equation 8 in §4.2.

To compute the expected number of bursts within the detection gap, we perform simulations using subsamples of bursts from Catalog 2, explicitly accounting for the effect of elevated sky temperature. To ensure approximately uniform exposure and sensitivity, we select all Catalog 2 bursts in the similar declination range of $30^\circ < \delta < 50^\circ$, resulting in 921 bursts. This sample serves as an empirical proxy for the intrinsic burst sample seen at this declination range in the absence of the influence of Cygnus X. From §3.1, the expected number of bursts originating behind the gap (i.e., before accounting for the elevated T_{sky} in the Cygnus X region) is 19, following a Poisson distribution. We generate 10^6 simulated realizations as follows:

- Generate a number of bursts originating behind the gap N_{gap} , drawn from a Poisson distribution $P(\lambda = 19)$;
- Randomly select N_{gap} bursts from the Catalog 2 subsample of 921 bursts, using their intrinsic burst width (W_i), sky temperature corresponding to their positions $T_{\text{sky},i}$ and signal-to-noise $(S/N)_i$ as burst parameters;
- Compute the (S/N) resulting from the changed sky temperature in the gap, as:

$$(S/N)_{\text{Cygnus}} = (S/N)_i \frac{T_{\text{sky},i} + T_{\text{sys}}}{T_{\text{sky,Cygnus}} + T_{\text{sys}}};$$

- For each realization, find the number of bursts detected in the gap, $N_{\text{detected,gap}}$, such that $(S/N)_{\text{Cygnus}} \geq 8$.

From the simulations, we find the mean number of bursts detected would be $\langle N_{\text{detected,gap}} \rangle = 6$, when accounting for the above-average T_{sky} . We find that zero detections occur in

fewer than 0.3% of the simulations (i.e., $N_{\text{detected,gap}} = 0$), indicating that increased sky temperature and Poisson fluctuations alone are insufficient to account for the observed gap towards Cygnus X.

4. ASSESSING POSSIBLE ORIGINS FOR THE DETECTION GAP

Cygnus X is one of the most massive star forming complexes in the Milky Way, rich in ionized gas. While it is possible that the spatial gap occurs by chance from the increased sky temperature, additional plasma processes are likely at play. Nominally, NE2001 predicts that the maximum DM through the region is $\approx 500 \text{ pc cm}^{-3}$, and maximum scattering timescale in CHIME’s observing band is $\tau_{\text{sc},600\text{MHz}} \approx 1.4 \text{ ms}$, comparable to the time sampling. These values are too small to cause appreciable DM smearing, or reduced S/N from scattering. However, angular broadening measurements of pulsars and a background FRB support a view in which Cygnus X is far more plasma rich than in existing Galactic electron models; in this Section we cover the existing literature, and investigate the gap in context of other observations through Cygnus X.

4.1. Background on the Cygnus X region

While Cygnus X is comprised of many distinct star forming regions, studies of molecular line observations have argued that they are associated, and at a similar distance d_{Cyg} (N. Schneider et al. 2006). This association was later supported using parallax measurements with masers (K. L. J. Rygl et al. 2012), and with Gaia (S. R. Berlanas et al. 2019), finding distance measurements spanning a range $1.3 < d_{\text{Cyg}} < 1.7 \text{ kpc}$. We adopt a value of $d_{\text{Cyg}} = 1.5 \text{ kpc}$ throughout our work (following discussion of F. Comerón et al. 2020), but emphasize that it does not strongly affect our analysis. At $d_{\text{Cyg}} = 1.5 \text{ kpc}$, the $\sim 18^\circ$ angular diameter of the spatial gap corresponds to $\sim 250 \text{ pc}$. Additionally, the electron temperature T_e is a function of Galactocentric radius R_{gal} , fit by C. Quireza et al. (2006) as $T_e(\text{K}) = (5780 \pm 350) + (287 \pm 46)R_{\text{Gal}}$. We adopt $T_e = 8000 \text{ K}$ throughout for the Cygnus X region, appropriate for $R_{\text{Gal}} \approx 8 \text{ kpc}$.

4.1.1. Emission Measure

From the Planck emission measure (EM) map (Planck Collaboration et al. 2016), which traces the free-free emission from ionized gas and has a resolution of $13.7' \approx 3 \text{ pc}$, the maximum EM of the Cygnus X region is 9400 pc cm^{-6} . On smaller angular scales, the Cygnus X region contains many thin filamentary structures, which are overdense and overpressured compared to the average properties of their surroundings (K. L. Emig et al. 2022). The maximum EM in these filaments approaches 10^5 pc cm^{-6} with a median

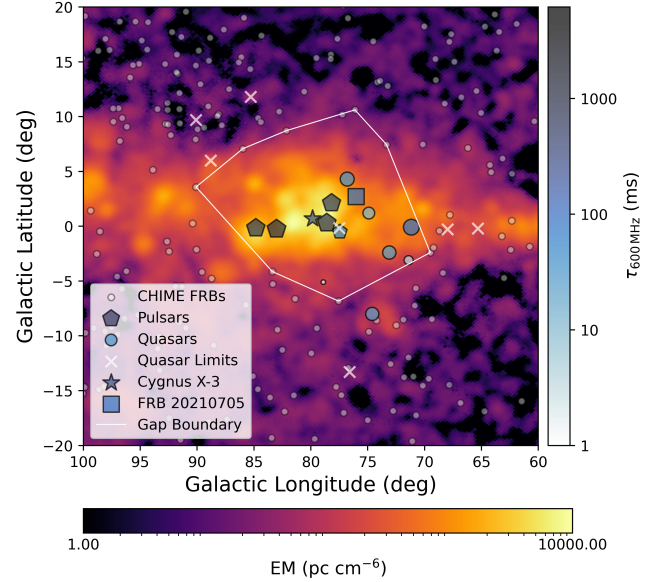


Figure 2. A comparison of literature values of scattering in and surrounding the Cygnus X region, as described in §4.1, overlaid on the Planck emission measure map (Planck Collaboration et al. 2016). The angular broadening measurements for quasars and Cygnus X-3 have been converted to scattering timescales using Equation 7, and scaled to 600 MHz using $\theta \propto \nu^{-2}$. Scattering measurements for pulsars and FRB 20210705 are extrapolated to 600 MHz using $\tau \propto \nu^{-4}$. This shows that sightlines through the Cygnus X region can produce ~ 10 – $1,000 \text{ ms}$ of temporal scattering in CHIME’s observing band, which would hinder detection of an FRB (see §4.4). A white polygon encloses the area with zero FRB detections, formed by Delaunay triangulation as described in §3.

value of 5200 pc cm^{-6} , and electron densities of $n_e \approx 10$ – 400 cm^{-3} , compared to the median of $n_e \approx 35 \text{ cm}^{-3}$. The density of the volume-filling ionized gas in the region is $n_e \approx 35 \text{ cm}^{-3}$, which itself is far above the volume-averaged plasma density in the WIM of $n_e \approx 0.03 \text{ cm}^{-3}$ (P. O. Mezger 1978; K. L. Emig et al. 2022).

The observables $\text{DM} = \int_0^L n_e(l) dl$ and $\text{EM} = \int_0^L n_e(l)^2 dl$ are physically related quantities where $n_e(l)$ is the free electron density (in cm^{-3}) at a distance l (in pc) along the line of sight, and L is the total path length through the ionized medium (in pc). Following S. K. Ocker et al. (2024), we assume that a path length L with volume-average electron density n_e is filled with dense cloudlets with a volume filling factor $f \leq 1$, and internal density $n_{e,i}$, such that $n_e = f n_{e,i}$. The other parameters are the variance of electron density within a cloudlet $\epsilon^2 = \langle (\delta n_{e,i})^2 \rangle / n_{e,i}^2 \leq 1$, and between cloudlets $\zeta = \langle n_{e,i}^2 \rangle / \langle n_{e,i} \rangle^2 \geq 1$. Following this prescription, the DM and EM are related as

$$\text{DM} = \sqrt{\frac{f}{\zeta(1+\epsilon^2)}} \text{EM} \times L. \quad (6)$$

The prefactor $\frac{f}{\zeta(1+\epsilon^2)}$ is always ≤ 1 , forming an upper limit on the DM.

Based on the above, a source seen through Cygnus X at the maximum EM $\approx 10^4 \text{ pc cm}^{-6}$ (from the Planck map) with path length $L \approx 500 \text{ pc}$ could accrue DM $\sim 2200 \text{ pc cm}^{-3}$. As will be described in §4.1.3, §4.1.4, this estimate is in line with the highest DMs of pulsars in the region, and that of the background FRB 20210705 discovered at L-band with the Five-hundred-meter Aperture Spherical radio Telescope (FAST). As discussed in §4.1.1, the peak EM in filaments reaches 10^5 pc cm^{-6} , although most filaments have thickness on the order of a few pc (K. L. Emig et al. 2022). A sightline could, in principle, accumulate a larger DM if it is seen directly through the long axis of a filament, but this is unlikely, and not representative of an average line-of-sight through the Cygnus X region.

4.1.2. Angular Broadening

Background quasars, if intrinsically compact enough, can show signs of angular broadening when observed through multi-frequency very long baseline interferometry (VLBI), characterized by broadening $\theta \propto \nu^\alpha$, scaling with $\alpha \approx -2$. Early VLBI observations of background quasars show angular broadening with full-width at half-maximum (FWHM) of $\theta_{\text{FWHM}} \approx 10 - 200 \text{ mas}$ referenced to 1 GHz within Galactic longitudes $60^\circ \lesssim l \lesssim 80^\circ$, greater than the surroundings (A. L. Fey et al. 1989, 1991). Observations of Cygnus X-3 (not associated with, but background to the Cygnus X region), show scatter broadening of 220–250 mas at 1 GHz (L. A. Molnar et al. 1995). Many additional VLBI studies of quasars through Cygnus X (e.g. T. J. W. Lazio & A. L. Fey 2001; K. M. Desai & A. L. Fey 2001; K. É. Gabányi et al. 2006) show angular broadening of a similar order, as well as extreme scattering event-like structures seen in the light-curve of quasar B2005+403, implying $\sim 0.7 \text{ AU}$ plasma structures (T. A. Koryukova et al. 2023).

Angular broadening, combined with the known distance to Cygnus X, can be used to predict the scattering time delay. For a scatter-broadened image with θ_{FWHM} , the scattering timescale τ_{sc} , defined as the $1/e$ timescale for a decaying exponential, is related to θ_{FWHM} as (e.g. J. M. Cordes & S. Chatterjee 2019):

$$\tau_{\text{sc}} \approx \frac{d_{\text{eff}} \theta_{\text{FWHM}}^2}{8 \ln(2) c}, \quad (7)$$

where $d_{\text{eff}} \equiv \frac{d_{\text{scr}}(D - d_{\text{scr}})}{D}$, for a scattering screen at distance d_{scr} from the observer and source at distance D . For an extragalactic source and a thin screen near the observer, $d_{\text{scr}} \ll (D - d_{\text{scr}})$, and $d_{\text{eff}} \approx d_{\text{scr}}$

This equation is exact for an angular intensity distribution following a Gaussian, and can differ by a factor of $\approx 0.6 - 2$

depending on the exact form of the scatter-broadened image. Scattering timescales derived for background radio sources using Equation 7 with $d_{\text{scr}} = d_{\text{Cyg}}$, are listed in Table 1.

4.1.3. Pulsars

There are > 90 known pulsars within our detection gap (R. N. Manchester et al. 2005). With surveys from more sensitive telescopes, many newly discovered pulsars in this region have DMs greater than the full expected Milky Way contribution from Galactic- n_e models (J. L. Han et al. 2025), as the abundance of plasma within Cygnus X is not properly accounted for. Without a reliable n_e model along these sightlines, and with few independent distance measurements, it is difficult to know which pulsars are foreground or background to the star-forming complex. As the complex itself is likely the cause of the discrepancy, the sources with DMs far exceeding model predictions can be assumed to be within or behind Cygnus X.

The FAST telescope recently measured scattering of 17 pulsars within our detection gap, spanning a range of $\tau_{\text{sc}, 1 \text{ GHz}} \approx 1 - 300 \text{ ms}$, and DMs $200 - 950 \text{ pc cm}^{-3}$ (W. C. Jing et al. 2025). Other pulsars with scattering measurements include PSR J2108+5001 discovered by the CHIME All-sky Multi-day Pulsar Stacking Search (The CHAMPSS Collaboration et al. 2025) located just outside of our detection gap boundary, and 9 pulsars discovered with the Green Bank Telescope (GBT) at 820 MHz (A. E. McEwen et al. 2024).

The maximum DM predicted by NE2001 and YMW16 at the center of the detection gap is $\sim 500 \text{ pc cm}^{-3}$. Pulsars with DMs exceeding this value are almost certainly located within or behind Cygnus X. Their scattering timescales can therefore provide an estimate of the propagation effects experienced by background sources, including FRBs intersecting this region. A list of the literature scattering measurements for DM $> 500 \text{ pc cm}^{-3}$ pulsars across the Cygnus X region is compiled in Table 1 and in Figure 2 (including J2108+5001 (482 pc cm^{-3}) which falls just below this threshold but as a CHIME-detected pulsar is relevant to the context of CHIME’s observing capabilities).

4.1.4. FRBs at Higher Observing Frequencies

According to Blinkverse (J. Xu et al. 2023), a single FRB lies within the CHIME detection gap: FRB 20210705 (see Figure 2), discovered by FAST in the Galactic Plane Pulsar Snapshot survey at L-band (D. J. Zhou et al. 2023). This burst is located at Galactic coordinates ($76.03^\circ, 2.71^\circ$) with DM $= 2011.6 \pm 3.2 \text{ pc cm}^{-3}$ and $\tau_{\text{sc}, 1 \text{ GHz}} = 12 \pm 2 \text{ ms}$ ($\tau_{\text{sc}, 600 \text{ MHz}} \approx 92 \pm 15 \text{ ms}$).

The distribution of observed scattering timescales in Catalog 2 is well-described by a log-normal distribution (CHIME/FRB Collaboration et al. 2025). In log-space, $\log_e(\tau_{\text{sc}}/\text{ms})$ follows a normal distribution characterized by

a mean $\mu = -0.52$ and standard deviation $\sigma = 1.01$. This corresponds to a mean $\tau_{\text{sc}, 1 \text{ GHz}} = 1 \text{ ms}$ and $\sigma = 1.32 \text{ ms}$. FRB 20210705 with $\log_e(\tau_{\text{sc}}/\text{ms}) = 2.48$, lies 2.97σ above the mean. This value corresponds to the 99.5th percentile of the Catalog 2 distribution, placing it among the most highly scattered FRBs in the sample.

We include all aforementioned measurements of angular broadening, and scattering timescales in Figure 2, superimposed on the Planck foreground EM map, surrounding our spatial gap in FRB detections.

4.2. Biases from DM Models and Dispersion Smearing

As described in §2.3, the CHIME/FRB backend classifies signals as Galactic, ambiguous, or extragalactic based on their position and DM, with extragalactic FRBs identified when their DMs exceed the maximum Galactic contributions predicted by the NE2001 and YMW16 models. Structural complexity of the ISM in the Milky Way plane leads to greater uncertainty in dispersion and scattering predicted by these models at lower Galactic latitudes compared to lines of sight at higher Galactic latitudes. In principle, these uncertainties could lead to misclassifications of FRBs as instead arising from Galactic sources due to an overestimation of the Galactic DM along the LOS by available models. The FRB 20220319D, detected and precisely localized at a distance of 50 Mpc by the Deep Synoptic Array (DSA-110), is one such example. It exhibits a DM ($110.95 \text{ pc cm}^{-3}$) lower than those predicted by the NE2001 (132.9 pc cm^{-3}) and YMW16 (187.7 pc cm^{-3}) models (V. Ravi et al. 2025) for extragalactic objects along its LOS ($l = 129.2^\circ$, $b = 9.1^\circ$). This highlights how overestimated model DMs may hinder the detectability of nearby, low-DM FRBs in pipelines with DM-based filtering. As discussed in §4.1.3, studies of pulsars in the background of Cygnus X have shown that the Galactic- n_e models instead make it more likely that unknown pulsars in the detection gap with unusually high DMs might be misclassified as FRBs.

We acknowledge the possibility that the Cygnus X complex is so poorly accounted for in the models that they could underestimate the maximum DM by an order of magnitude, i.e., that the true value of $\text{DM}_{\text{max}} \geq 5000 \text{ pc cm}^{-3}$ along the LOS. At such high DMs, intra-channel dispersion smearing could partially emulate scatter-broadening and reduce pulse brightness at low frequencies. However, we believe that DM smearing can be ruled out as the origin of the detection gap. Temporal broadening due to intra-channel dispersion smearing (J. M. Cordes & M. A. McLaughlin 2003) is given by:

$$t_{\text{chan}} = 8.3 \mu\text{s} \left(\frac{\Delta\nu_{\text{chan}}}{\text{MHz}} \right) \left(\frac{\nu}{\text{GHz}} \right)^{-3} \left(\frac{\text{DM}}{\text{pc cm}^{-3}} \right). \quad (8)$$

The CHIME/FRB detection pipeline searches to a maximum DM of 13000 pc cm^{-3} (CHIME/FRB Collaboration

et al. 2018). In order to produce $t_{\text{chan}} \approx 8 \text{ ms}$ at 600 MHz – comparable to the mean value of τ_{sc} measured in Catalog 2 (1 ms at 1 GHz; see §4.1.4) – a value of $\text{DM} > 8000 \text{ pc cm}^{-3}$ is required. This estimate is nearly an order of magnitude higher than the DM inferred from the maximum EM in the Cygnus X region as discussed in §4.1.1.

4.3. Free-free Absorption in the Direction of Cygnus X

Here, we examine whether the FRB detection gap towards Cygnus X could be caused by free-free absorption. The free-free opacity is well approximated by (P. G. Mezger & A. P. Henderson 1967)

$$\tau_{\text{ff}} = 3.28 \times 10^{-7} \left(\frac{T_e}{10^4 \text{ K}} \right)^{-1.35} \left(\frac{\nu}{\text{GHz}} \right)^{-2.1} \left(\frac{\text{EM}}{\text{pc cm}^{-6}} \right), \quad (9)$$

As discussed in §4.1, the Planck EM map for the Cygnus X region indicates that $\text{EM} \approx 9400 \text{ pc cm}^{-6}$, while detailed studies of overdense and overpressured filaments show peak values of $\text{EM} \approx 10^5 \text{ pc cm}^{-6}$ K. L. Emig et al. (2022).

Inserting $\text{EM} \approx 10^4 \text{ pc cm}^{-6}$ for the Cygnus X region (S. K. Ocker et al. 2024), and $T_e \approx 8000 \text{ K}$, the opacity is $\tau_{\text{ff}} \approx 0.02$ at $\nu = 400 \text{ MHz}$, the bottom of our band. For the maximum measured emission measures of $\text{EM} \approx 10^5 \text{ pc cm}^{-6}$, free-free absorption begins to matter, with $\tau_{\text{ff}} \approx 0.2$ at $\nu = 400 \text{ MHz}$, but still a small effect, and with $\tau_{\text{ff}} < 0.1$ averaged across the band. The detection of background quasars at 350 MHz (e.g. T. J. W. Lazio & A. L. Fey 2001), and prevalence of free-free emission at 148 MHz (e.g. K. L. Emig et al. 2022) also qualitatively suggests that free-free absorption is not dominating at low radio frequencies in this region. We therefore conclude that while free-free absorption could have a small effect on a background FRB, it is not the primary cause of the detection gap.

4.4. Empirical Limits on Scattering Timescale

As summarized in §4.1, the measurements to date of sources observed through the Cygnus X region – through angular broadening of background quasars and Cygnus X-3, scattering of distant pulsars and one FRB detected by FAST – show significant scattering ($\tau_{\text{sc}, 600 \text{ MHz}} \sim 10 - 1000 \text{ ms}$). This already suggests that scattering can be deleterious for FRB detections at CHIME, and is likely a significant contributor to the lack of CHIME/FRB detections in the gap. However, the magnitude of scattering, which depends on plasma fluctuations on tiny scales at $\ll \text{AU}$, can drastically differ between sightlines. In this Section, we quantify the effect of scattering on CHIME/FRB detections, and in turn set a lower limit on the average scattering in the detection gap which would lead to zero detections.

We first searched the positional and `fitburst` data in Catalog 2 for a radial trend in measured τ_{sc} from the boundary of the Cygnus X region, observing no clear trend. In Cat-

alog 1 injections, CHIME/FRB found a strong selection bias against temporally broad bursts ($W_b > 10$ ms, calculated at 600 MHz; M. Merryfield et al. 2023). The lack of a trend may be due to the narrow observable window in τ_{sc} : the lower limit set by the reliability cut-off (see §2.4; 0.13 ms at 1 GHz); and the upper limit (≥ 10 ms at 1 GHz) that corresponds to scattered pulses likely too broad to detect. Along with a limited number of detected FRBs, a statistically significant radial trend is difficult to establish without finer time resolution to probe a wider range in τ_{sc} . As a result, it is difficult to trace if there is a gradual increase in scattering timescales for sightlines closer to the center of the detection gap.

From the simulations described in §3.2, we found that on an average 6 bursts are expected to be seen in the detection gap. These simulations account for the elevated sky temperature but not for scattering. Here, we extend the simulation to assess the degree of scattering required to see zero bursts.

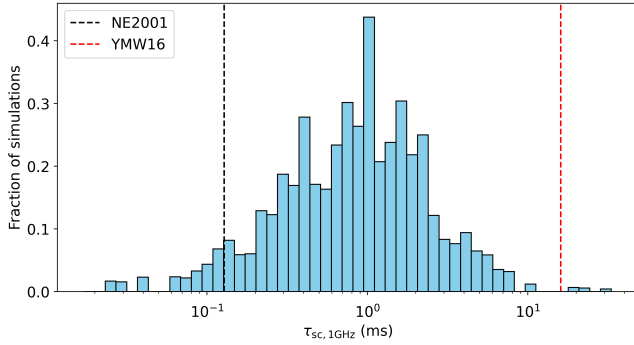


Figure 3. Distribution of scattering timescales at 1 GHz that result in zero detectable FRBs in the gap across 10^6 simulations, incorporating elevated sky temperature as described in §3.2. Vertical dashed lines indicate scattering predictions from the NE2001 model (black) and YMW16 model (red) for the line of sight along the center of the gap.

In the simulations outlined in §3.2, we introduce pulse broadening due to scattering using Equation 5. For each simulated realization, we compute the minimum τ_{sc} using Equation 4, such that the increased W_b and T_{sky} reduce the signal-to-noise of all FRBs within the detection gap to $(S/N)_b < (S/N)_{\text{thresh}} = 8$. The distribution of $\tau_{sc, 1\text{GHz}}$ values obtained from these simulations is shown in Figure 3. We find that a mean value of $\tau_{sc, 1\text{GHz}} = 4.13$ ms, or $\tau_{sc, 600\text{MHz}} = 31.87$ ms is sufficient to suppress all detections. The maximum τ_{sc} predicted by Galactic- n_e models for the LOS through the center of the detection gap are: $\tau_{sc, 1\text{GHz}}^{\text{NE2001}} = 0.1$ ms and $\tau_{sc, 1\text{GHz}}^{\text{YMW16}} = 16$ ms. This range of model-dependent maximum values of τ_{sc} is consistent with our inferred maximum derived from the simulations. Moreover, this consistency reinforces the idea that enhanced scattering in Cygnus X is likely to explain the detection gap, though our limit was obtained in a man-

ner independent of either n_e model. However, we emphasize that these models are outdated, differ in their treatment of the Cygnus X region¹⁹, and lack accurate modeling of small-scale plasma fluctuations, so their predictions should be interpreted only as rough references.

5. DISCUSSION

The statistical significance of the detection gap was aided by its large angular extent, as discussed in §3.1. Smaller spatial gaps however, can occur through chance. We used the non-detections of FRBs in the direction of Cygnus X to place data-driven constraints on the magnitude of maximal scattering from the Milky Way Galaxy, in a manner independent of existing Galactic- n_e models. However, even if smaller in angular extents, other ionized structures in the Galaxy such as H II regions and high-EM sightlines may have similar impacts on the observed scattering properties and detectability of FRBs in Catalog 2. This may introduce a selection bias in observed FRB environments, potentially skewing interpretations of their host galaxy associations.

The Murchison Widefield Array Interplanetary Scintillation survey has revealed similar spatial gaps in the distribution of compact radio sources due to angular broadening from clumpy ISM turbulence correlated with H α emission (J. S. Morgan et al. 2022). In the case of pulsars, scintillation arcs and VLBI have been used to localize scattering structures to known H II regions (e.g. G. Mall et al. 2022).

Figure 4 provides a visual overview of the spatial relationship between Catalog 2 FRBs, known H II regions, and EM. Several FRB sightlines in our sample intersect known H II regions. Furthermore, Figure 4 illustrates the possibility that FRBs with significant scattering are more likely to occur along lines of sight intersecting H II regions – or be missed entirely due to reduced detectability. These visual trends in the sky distribution of Catalog 2 FRBs motivates the discussion in the following subsections.

5.1. Trends with DM, EM, and H α

To statistically test whether highly scattered FRBs are under-detected in general due to propagation through regions of elevated emission measure, we compared EMs at FRB positions with those along all sightlines visible to CHIME. Exposure weighting is applied using the CHIME/FRB beam exposure map (CHIME/FRB Collaboration et al. 2025), such that each sky position contributes proportionally to its observing time. Figure 5 shows this comparison using the Planck EM map (Planck Collaboration et al. 2016). The FRB distribution drops to zero for $\text{EM} \geq 2900$ pc cm⁻⁶. This dif-

¹⁹ For example, the YMW16 model does not incorporate external information available on the Cygnus X complex.

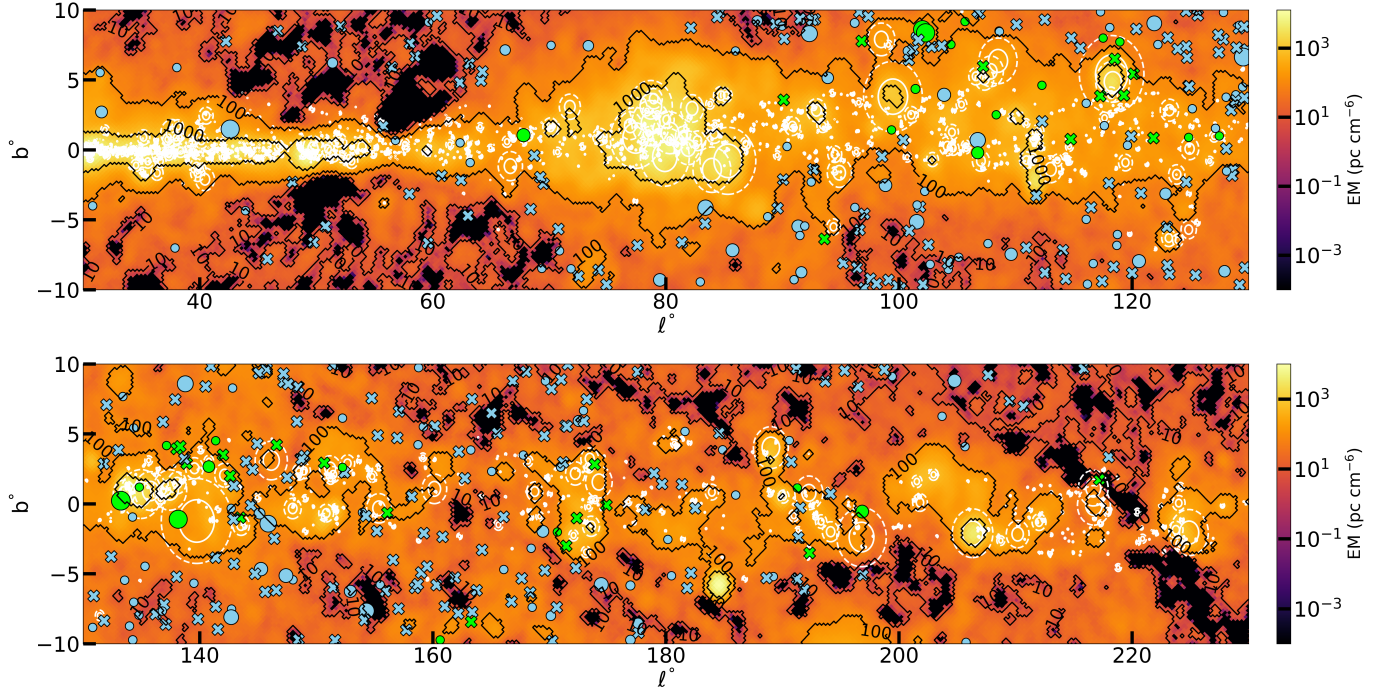


Figure 4. Planck EM map (Planck Collaboration et al. 2016) in Galactic coordinates centered at $l = 80^\circ$, $b = 0^\circ$ (top) and $l = 180^\circ$, $b = 0^\circ$ (bottom). Overlaid black contours trace logarithmically-spaced EM 10, 100 and 1,000 pc cm^{-6} . White solid and dashed circles highlight WISE H II regions (L. D. Anderson et al. 2014) with angular radii θ_{IR} and $2\theta_{\text{IR}}$, respectively. The radius of the IR emission θ_{IR} is provided by the WISE Catalog. H II regions from the HH14 catalog (L. G. Hou & J. L. Han 2014a) are not shown in this figure as their angular radii are not available but FRBs intersecting them are included (see §5.2 for the treatment). Lime markers are for FRB LOS with intersecting H II regions and skyblue markers are for non-intersecting FRBs. Cross markers indicate FRBs for which no reliable scattering timescale was measured with total-intensity data, while the radii of circular FRB markers are scaled according to the log of the measured scattering timescale.

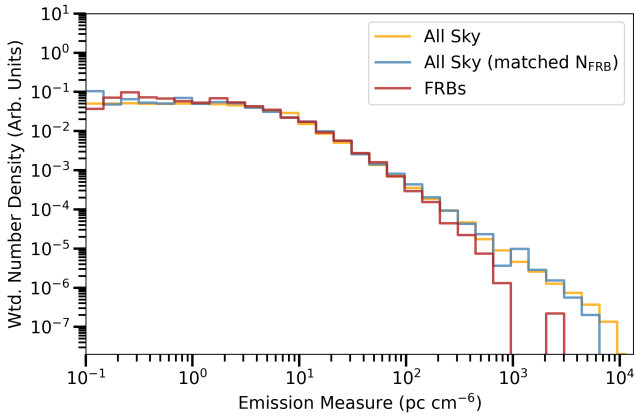


Figure 5. Normalized, exposure weighted (wtd.) number density histogram of emission measures along all CHIME/FRB sightlines (orange) compared to the EM distribution at detected FRB positions (red). The ‘All Sky (matched N_{FRB})’ (blue) curve corresponds to EMs along the same number of sightlines as the FRB sample, uniformly distributed in the CHIME-visible sky. This control sample is plotted to assess whether the apparent deficit of FRBs along high-EM sightlines arises from small-number statistics rather than a physical suppression. The y-axis is plotted in arbitrary (arb.) units for ease of comparison between samples.

ference demonstrates a deficit of FRBs along high EM sightlines that are associated with ionized regions in the Galaxy.

We can ask what the above EM cutoff of 2900 pc cm^{-6} corresponds to in terms of τ_{ff} , DM, and τ_{sc} . Similar to the calculations in §4.3, τ_{ff} is negligible (≈ 0.003) in our band. Using Equation 6, and assuming $L = 40 \text{ pc}$ (a characteristic H II region path length corresponding to typical Strömgen diameter for O8-B0 stars; see §5.2), we estimate a DM contribution near the cutoff of $\approx 340 \text{ pc cm}^{-3}$, which is too small to induce appreciable DM smearing. We estimate τ_{sc} using the empirical τ_{sc} –DM relation from J. M. Cordes et al. (2016), resulting in a rough lower bound of $\tau_{sc, 1\text{GHz}} \gtrsim 0.5 \text{ ms}$, or $\tau_{sc, 600\text{MHz}} \gtrsim 4 \text{ ms}$. We note that use of their relation while assuming $\text{DM} \propto \sqrt{\text{EM}}$ yields $\tau_{sc} \propto \text{EM}^{2.25}$ for $\text{DM} \gtrsim 100 \text{ pc cm}^{-3}$; values of EM above the aforementioned cutoff yield values of τ_{sc} that rapidly rises to magnitudes that make FRBs undetectable at CHIME. We also note that pulsars behind H II regions lie preferentially above the τ_{sc} –DM relation and that a future reassessment is therefore warranted (S. K. Ocker et al. 2024). While we caution that the logic mapping EM to τ_{sc} is indirect, the above results support the interpretation that FRBs are preferentially scatter-broadened beyond detectability along high EM sightlines.

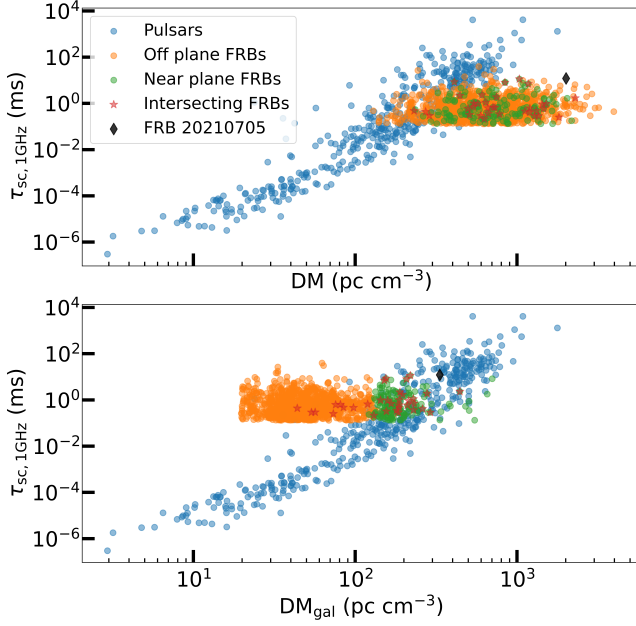


Figure 6. Catalog 2 FRBs plotted alongside pulsars and FRB 20210705 in the τ -DM plane. Top panel: $\tau_{\text{sc},1\text{GHz}}$ versus total DM. Bottom panel: $\tau_{\text{sc},1\text{GHz}}$ versus Galactic DM contribution. In both panels, blue points show Galactic pulsars, green points show FRBs near the Galactic plane ($|b| < 10^\circ$) and orange points mark those away from the plane. Red star markers show FRBs intersecting known H II regions and black diamond marks the FRB 20210705.

5.2. H II Region Intersections and Scattering Properties

Similar to the treatment for pulsar sightlines intersecting H II regions by [S. K. Ocker et al. \(2024\)](#), we utilize 2 complementary catalogs of H II regions – WISE V2.4 ([L. D. Anderson et al. 2014](#)) and HH14 ([L. G. Hou & J. L. Han 2014a](#)), as together they span radio, infra-red (IR) and optical wavelengths. The WISE catalog contains over 8,400 H II regions and H II region candidates, identified using the all-sky Wide-field Infrared Survey Explorer (WISE) satellite data. The HH14 catalog contains 4,551 H II regions, of which 611 have spectro-photometric distance measurements. Although HH14 does not provide angular radii of H II regions, we adopt the maximum impact parameter 20 pc from [S. K. Ocker et al. \(2024\)](#) based on typical Strömgren radii for O8-B0 stars and we then scale the angular extents based on the distances of corresponding H II regions provided in the catalog.

We match FRBs to WISE H II regions by computing angular separations in Galactic coordinates and checking whether each FRB falls within twice the angular radius of any H II region ($< 2\theta_{\text{IR}}$). We adopt this maximum impact parameter of $2\theta_{\text{IR}}$ following the prescription of [S. K. Ocker et al. \(2024\)](#) to account for potential underestimation of the ionized gas extent by the infrared size, which may miss diffuse outer emission caused by radiation leakage ([M. Luisi et al. 2019](#); [J. Dey](#)

[et al. 2024](#)). Out of the 3552 FRBs in our sample, 36 FRB sightlines pass through WISE H II regions and 85 sightlines pass through HH14 H II regions, with 11 sightlines in common between them, making a total of 110.

Among FRB sightlines that intersect H II regions, as well as those that do not but lie near the Galactic plane ($|b| < 10^\circ$), only about one-third pass the τ_{sc} reliability cut off described in §2.4. This sample of sightlines is not sufficiently large to enable a robust statistical comparison of τ_{sc} between these subsets. For completeness, we report the mean and median $\tau_{\text{sc},1\text{GHz}}$ values: for intersecting sightlines, the mean is 1.68 ms and the median is 0.63 ms; for non-intersecting near-plane sightlines, the mean is 1.05 ms and the median is 0.53 ms. The intersecting sample exhibits slightly higher values consistent with expectations, but an AD-test between the two populations yields a statistic of 1.58 and a p -value of 0.07 indicating no significance. A more robust assessment will require either a larger sample from future CHIME/FRB catalogs or the use of raw baseband data with its higher time resolution to permit measurement of shorter scattering timescales. For interested readers, Table 2 in Appendix B lists the FRB sightlines that intersect H II regions, along with their positions, DMs, and τ_{sc} . These may be useful for further case studies of scattering in dense Galactic environments. Their dynamic spectra are presented in Figure 7 in Appendix B to illustrate observed pulse morphologies.

For future investigation, we point out two interesting candidates. The FRB 20190912D LOS passes through the Sharpless 171 (S171) H II region surrounding the Berkeley 59 cluster of young stars. The FRB 20200416A LOS passes through the giant W4 complex enclosing the Heart Nebula, hosting numerous O/B-type stars and the IC1805 open cluster of young stars. Interestingly, the *fitburst*-measured τ_{sc} for FRB 20200416A is smaller than the maximum predicted by NE2001 for an extragalactic source along this LOS. This could indicate an overestimate by the model, or geometric suppression of scattering if the dominant screen lies at a cosmological distance/closer to the observer. However, we note that NE2001 was not designed to predict scattering with high precision, especially for extragalactic sources and along complex or poorly constrained sightlines. As such, this comparison should be interpreted cautiously.

We also explore the possibility of a correlation or lack thereof between τ_{sc} and DM for FRBs. Figure 6 shows a τ_{sc} -DM plot for all FRB candidates in Catalog 2, and exhibits an overall trend that confirms previous findings – FRBs are systematically under-scattered compared to expectations from the τ_{sc} -DM relation from Galactic pulsars ([J. Cordes et al. 2016](#)). The discrepancy arises because a large fraction of the FRB DM comes from the intergalactic medium, which contributes minimally to scattering ([D. R. Lorimer et al. 2007](#); [D. Thornton et al. 2013](#)). However, this comparison is bi-

ased to reflect the statistics of detected events as we likely miss highly scattered FRBs passing through H II regions that therefore fall below the CHIME/FRB detection threshold. For example, Catalog 2 FRBs that intersect Galactic H II regions do not show a strong correlation between DM and τ_{sc} in Figure 6 for FRBs – even when considering only the Galactic contribution to DM – despite the expectation that significant δn_e in H II regions causes scattering. However, FRB 20210705 as detected by the FAST telescope (see discussion in §4.1.4) indeed follows the τ_{sc} –DM trend, indicating that its scattering is consistent with being induced by the Cygnus X region. While the statistics currently remain small, this difference raises a cautionary note for population studies: low scattering, high DM bursts may be overrepresented in Catalog 2. CHIME/FRB’s selection function for Catalog 1 has been studied by injecting synthetic FRBs (M. Merryfield et al. 2023). This effort confirmed that the CHIME/FRB backend is more sensitive to bursts with smaller broadened pulse widths. An updated injections study for Catalog 2 is currently underway. In order to make conclusions about the cosmological population of FRBs, a follow-up study incorporating the updated selection functions and host models is essential.

5.3. Visibility Fitting of Scattered FRBs as a Complementary Probe of ISM Scattering

As discussed in 4.1.2, a scattered source will also be angularly broadened, where larger time delays correspond to larger deflection angles. Assuming $d_{\text{eff}} \approx d_{\text{scr}}$ for an extragalactic source, the mapping between delay τ and observed angle θ for each scattered path through a thin screen is (e.g. M. A. Walker et al. 2004)

$$\theta = \sqrt{\frac{2c\tau}{d_{\text{scr}}}} \approx 91 \text{ mas} \left(\frac{\tau}{10 \text{ ms}} \right)^{1/2} \left(\frac{d_{\text{scr}}}{1 \text{ kpc}} \right)^{-1/2}. \quad (10)$$

The CHIME/FRB Outriggers project (CHIME Collaboration et al. 2025) augments CHIME/FRB by providing milliarcsecond-scale localization using VLBI across three strategically placed stations in North America. By enabling precise FRB localization, the Outriggers facilitate host galaxy identification, studies of FRB environments, and their use as cosmological probes. Given CHIME/FRB Outriggers’ target resolution of $\theta_{\text{res}} \approx 50 \text{ mas}$ (CHIME Collaboration et al. 2025), FRBs scattered by $\tau_{\text{sc}, 600 \text{ MHz}} \gtrsim 10 \text{ ms}$ at $\sim \text{kpc}$ distances will have an angular extent larger than the Outriggers’ resolution. Many of the bright bursts piercing through H II regions, or one detected through Cygnus X (with $\tau_{\text{sc}, 600 \text{ MHz}} \gtrsim 40 \text{ ms}$), would be easily resolved by CHIME/FRB Outriggers. We note that while CHIME/FRB is biased against finding bursts of these scattering times, particularly bright bursts are seen with sufficient scattering for this approach (e.g. see K. Shin et al. 2024 for a bright burst scattered $\gtrsim 1 \text{ s}$ in the CHIME band.)

Given the mapping between τ and θ , the interferometric visibility (V) of scattered FRBs (or pulsars) will show a characteristic shape as a function of $V(\tau, \nu)$ through a scattering tail (O. Wucknitz 2012, 2014), which allows for a determination of screen distances and orientations. Conversely, for spatially unresolved sources, an upper limit on the angular broadening will place a lower limit on the screen distance. This will allow mapping of Galactic scattering structures to astrophysical sources, and will cleanly distinguish between Galactic and extragalactic scattering screens.

Upcoming ultra-wideband instruments such as the Canadian Hydrogen Observatory and Radio Transient Detector (CHORD; 300–1500 MHz; K. Vanderlinde et al. 2019) and DSA-2000 (0.7–2GHz; G. Hallinan et al. 2019) will be particularly well-suited to studies of scattering, offering improved sensitivity across a broad frequency range.

6. CONCLUSION

Our analysis shows that FRB detections in CHIME/FRB Catalog 2 exhibit a two-dimensional dependence on Galactic coordinates. The most striking feature is the complete absence of CHIME/FRB detections in a patch of the sky that coincides with the Cygnus X region. The analyses discussed in §3–5 demonstrate that this detection gap, along with other regions of reduced FRB detections within the Galactic plane, correspond with known H II regions. Based on the discussion presented in §5, we favor the interpretation that turbulence along these lines of sight induces large degrees of scatter-broadening that totally smear FRBs out of detectability within the CHIME band. We note that measurements of τ_{sc} in CHIME/FRB Catalog 2 and derived τ_{sc} from non-detections could be used to gauge the accuracy of existing electron-density models of the Milky Way Galaxy.

Future CHIME/FRB measurements of τ_{sc} will increase the surface density of FRB detections at low frequencies. Such an increase will likely yield additional detection gaps associated with Galactic H II regions that have smaller angular extents. These same data sets will also allow for data-driven constraints on the Galactic electron density models themselves, through all-sky estimates of the maximum τ_{sc} as estimated for the Cygnus X region in §4.4. Although the nature of FRB classification makes similar constraints on DM more complicated, phenomenological models can be used to gauge the likely maximum values for the contribution of the Milky Way to DM (e.g., A. M. Cook et al. 2023). We therefore expect that future CHIME/FRB catalogs will provide the means to strengthen and expand upon the inferences made in our work.

The CHIME/FRB experiment is also recording baseband (voltage) data for the high-significance subset of its catalogs (D. Michilli et al. 2021). Access to baseband data allows for evaluation of polarization profiles (e.g., R. Mckin-

ven et al. 2023a,b, 2025; A. Pandhi et al. 2024), scattering-broadening at the sub-ms level (K. R. Sand et al. 2024; A. P. Curtin et al. 2024), and the presence of scintillation down to the Nyquist-limited data resolution (e.g., K. Nimmo et al. 2025). A catalog of such FRB measurements will provide novel avenues for exploring the structure of the WIM, e.g., using FRB scintillation as a tool to complement the analysis of intra-day scintillation of blazars coincident with Galactic $H\alpha$ emission (e.g., J. Y. Koay et al. 2019). These measurements may also be useful for exploring the impact of other Galactic features that interact with the WIM (e.g., the “Fermi bubbles;” M. Su et al. 2010; D. Krishnarao et al. 2020). Furthermore, future CHIME/FRB baseband catalogs will shed light on the role of scintillation in potentially affecting FRB detection rates across Galactic latitudes (J.-P. Macquart & S. Johnston 2015).

The CHIME/FRB experiment is also expanding its capabilities to measure the angular broadening of FRBs through Outriggers. Coupled with the time delay from scattering, this will enable the determination of the geometry of scattering screens. This additional constraint will be crucial for further probing the role of the WIM in modulating FRB visibility. This includes spatial correlations with known plasma structures such as H II regions, $H\alpha$ filaments, and detailed comparisons to emission and dispersion measures across the sky. This present work can therefore be viewed as a step towards using FRBs, both in the time and image domains, as “backlights” to explore the WIM of the Milky Way Galaxy.

ACKNOWLEDGEMENTS

We acknowledge that CHIME is located on the traditional, ancestral, and unceded territory of the Syilx/Okanagan people. We are grateful to the staff of the Dominion Radio Astrophysical Observatory, which is operated by the National Research Council of Canada. CHIME operations are funded by a grant from the NSERC Alliance Program and by support from McGill University, University of British Columbia, and University of Toronto. CHIME was funded by a grant from the Canada Foundation for Innovation (CFI) 2012 Leading Edge Fund (Project 31170) and by contributions from the provinces of British Columbia, Québec and Ontario. The CHIME/FRB Project was funded by a grant from the CFI 2015 Innovation Fund (Project 33213) and by contributions from the provinces of British Columbia and Québec, and by the Dunlap Institute for Astronomy and Astrophysics at the University of Toronto. Additional support was provided by the Canadian Institute for Advanced Research (CIFAR), the Trottier Space Institute at McGill University, and the University of British Columbia (UBC). This research has made use of the VizieR catalogue access tool, CDS, Strasbourg, France (DOI : 10.26093/cds/vizieR). The original description of the VizieR service was published in 2000, A&AS 143, 23.

We thank Dr. Duncan Lorimer, Dr. Liam Connor and Dr. Namir Kassim for thoughtful questions and discussions that informed the analysis presented in this paper.

E.F. and S.S.P. are supported by the National Science Foundation under grant AST-2407399. K.T.M. is supported by a FRQNT Master’s Research Scholarship. A.M.C. acknowledges funding from NSERC as a Banting Postdoctoral Fellow. A.P.C. is a Vanier Canada Graduate Scholar. G.M.E. acknowledges support from NSERC Discovery Grant RGPIN-2020-04554. V.M.K. holds the Lorne Trottier Chair in Astrophysics & Cosmology, a Distinguished James McGill Professorship, and receives support from an NSERC Discovery grant (RGPIN 228738-13). C. L. acknowledges support from the Miller Institute for Basic Research at UC Berkeley. K.W.M. holds the Adam J. Burgasser Chair in Astrophysics and is supported by NSF grant 2018490. M.N. is a Fonds de Recherche du Québec – Nature et Technologies (FRQNT) postdoctoral fellow. K.N. is an MIT Kavli Fellow. A.P. is funded by the NSERC Canada Graduate Scholarships – Doctoral program. A.B.P. is a Banting Fellow, a McGill Space Institute (MSI) Fellow, and a FRQNT postdoctoral fellow. Z.P. is supported by an NWO Veni fellowship (VI.Veni.222.295). M.W.S. acknowledges support from the Trottier Space Institute Fellowship program. K.R.S. acknowledges support from FRQNT doctoral research award. P.S. acknowledges the support of an NSERC Discovery Grant (RGPIN-2024-06266). K.S. is supported by the NSF Graduate Research Fellowship Program.

APPENDIX

A. LITERATURE SCATTERING VALUES NEAR CYGNUS X

Table 1. Table with literature values of scattering and angular broadening towards Cygnus X, from background pulsars, FRBs, quasars, and Cygnus X-3. References: [1] W. C. Jing et al. (2025), [2] The CHAMPSS Collaboration et al. (2025), [3] D. J. Zhou et al. (2022), [4] A. L. Fey et al. (1989), [5] A. L. Fey et al. (1991), [6] L. A. Molnar et al. (1995)

Source	ℓ (deg)	b (deg)	θ (mas)	$\tau_{1\text{GHz}}$ (ms)	$\tau_{600\text{MHz}}$ (ms)	Reference
PSR J2021+4024g	78.18	2.11	–	8.21e+01	6.33e+02	[1]
PSR J2030+3818g	77.45	-0.51	–	7.80	6.02e+01	[1]
PSR J2030+3944g	78.60	0.30	–	1.14e+02	8.80e+02	[1]
PSR J2046+4253g	83.02	-0.26	–	1.27e+02	9.80e+02	[1]
PSR J2052+4421g	84.84	-0.17	–	9.50e+01	7.33e+02	[1]
PSR J2108+5001	91.20	1.47	–	1.91	14.7	[2]
FRB 20210705	76.03	2.71	–	1.19e+01	9.20e+01	[3]
1923+210	55.60	2.30	<16.30	<1.74e-01	<1.34	[4]
1954+513	85.30	11.80	<4.30	<1.21e-02	<9.34e-02	[4]
2005+403	76.80	4.30	79.50	4.14	3.19e+01	[4]
2013+370	74.90	1.20	46.40	1.41	1.09e+01	[4]
2021+317	71.40	-3.10	25.70	4.32e-01	3.34	[4]
2022+542	90.10	9.70	<1.40	<1.28e-03	<9.90e-03	[4]
2023+336	73.10	-2.40	67.60	2.99	2.31e+01	[4]
2048+313	74.60	-8.00	64.70	2.74	2.11e+01	[4]
2050+364	78.90	-5.10	9.30	5.66e-02	4.37e-01	[4]
2113+293	76.60	-13.30	<1.20	<9.42e-04	<7.27e-03	[4]
3C418	88.80	6.00	<8.00	<4.19e-02	<3.23e-01	[5]
1922+155	50.62	-0.03	<20.00	<2.62e-01	<2.02	[5]
1932+204	56.08	0.10	<14.00	<1.28e-01	<9.90e-01	[5]
1934+207	56.55	-0.07	<9.60	<6.03e-02	<4.65e-01	[5]
1954+282	65.31	-0.21	<8.30	<4.51e-02	<3.48e-01	[5]
2001+304	67.97	-0.29	<13.60	<1.21e-01	<9.34e-01	[5]
2008+33D	71.16	-0.09	130.00	1.11e+01	8.53e+01	[5]
2027+383	77.50	-0.17	<189.00	<2.34e+01	<1.80e+02	[5]
Cygnus X-3	79.85	0.70	240	3.77e+01	2.91e+02	[6]

B. FRBS INTERSECTING H II REGIONS

B.1. *Catalog*

Table 2. A full list of FRB sightlines intersecting H II regions from the WISE (L. D. Anderson et al. 2014) and HH14 (L. G. Hou & J. L. Han 2014b) catalogs.

TNS Name	(l, b)	τ_{sc}	DM	Name	(l, b)	D	θ_{IR}	Catalog
	(deg)	(ms at 1 GHz)	(pc cm ⁻³)		(deg)	(kpc)	(deg)	
FRB20200306C	15.6, 28	–	337.2	–	6.4, 22.9	–	5.19	WISE
FRB20230511B	15.7, 23.1	–	191.6	–	6.4, 22.9	–	5.19	WISE

Table 2. Continued.

TNS Name	(l, b)	τ_{sc}	DM	Name	(l, b)	D	θ_{IR}	Catalog
	(deg)	(ms at 1 GHz)	(pc cm ⁻³)		(deg)	(kpc)	(deg)	
FRB20181119B	67.8, 1	2.307 ± 2.3	608.5	–	68.2, 1.1	–	0.22	WISE
FRB20210817B	90.1, 3.6	–	483.1	–	90.2, 2.3	–	–	HH14
FRB20221109A	93.6, -6.4	–	1580	–	94.4, -5.5	–	–	HH14
FRB20201225A	94.3, 18.6	–	145.6	–	95.4, 16.8	–	–	HH14
FRB20190211B	94.4, 16.1	–	260.7	–	95.4, 16.8	–	–	HH14
FRB20230727C	94.9, 17	–	700.8	–	95.4, 16.8	–	–	HH14
FRB20210503A	95.1, 14.8	–	388.3	–	95.4, 16.8	–	–	HH14
FRB20200514D	95.4, 18.7	0.252 ± 0.25	1819	–	95.4, 16.8	–	–	HH14
FRB20211117F	95.7, 14.7	–	1021	–	95.4, 16.8	–	–	HH14
FRB20221206I	96.8, 18.7	–	707.1	–	95.4, 16.8	–	–	HH14
FRB20210105A	96.8, 7.8	–	2470	–	98.5, 8	–	–	HH14
FRB20210129A	97.7, 16.1	–	632.2	–	95.4, 16.8	–	–	HH14
FRB20180918A	98.1, 17.1	–	1454	–	95.4, 16.8	–	–	HH14
FRB20230426F	99.4, 1.4	0.286 ± 0.29	1360	S131; IC1396	99.5, 3.8	0.91 ± 0.57	1.26	WISE
FRB20210810B	101.4, 4.4	1.101 ± 1.1	639.6	S131; IC1396	99.5, 3.8	0.91 ± 0.57	1.26	WISE
FRB20220822A	102, 8.6	6.995 ± 7	1174	–	103.1, 9.6	–	–	HH14
FRB20221214C	102.3, 8.4	8.46 ± 8.5	409.5	–	103.1, 9.6	–	–	HH14
FRB20210507B	104.3, 10.9	–	415.5	–	103.1, 9.6	–	–	HH14
FRB20211103D	104.4, 7.5	0.689 ± 0.69	711.1	–	105.6, 7.8	–	–	HH14
FRB20191213C	105.7, 9.2	0.982 ± 0.98	571.3	–	105.4, 9.9	–	–	HH14
FRB20200711E	106.5, 10.1	–	691.6	–	105.4, 9.9	–	–	HH14
FRB20210103A	106.7, -0.2	1.881 ± 1.9	746.2	S142	107, -0.8	3.52 ± 0.47	0.37	WISE
FRB20230102D	107.2, 6	–	983	–	107.9, 5.8	–	–	HH14
				S141	107.9, 5.6	–	0.55	WISE
				S150	108.5, 6.4	1.34 ± 0.47	0.82	WISE
				–	106.8, 5.3	–	–	HH14
FRB20200917B	108.3, 2.5	0.409 ± 0.41	1198	–	109.9, 2.1	–	–	HH14
FRB20230409B	112.3, 4.6	0.587 ± 0.59	1459	–	111.9, 4.1	–	–	HH14
FRB20210603D	114.7, 0.8	–	502.2	–	114.6, 0.2	–	–	HH14
FRB20230316H	117.3, 3.9	–	496.1	S171	118.2, 5.4	–	1.39	WISE
FRB20220411A	117.5, 8	0.323 ± 0.32	507.4	S171	118.2, 5.4	–	1.39	WISE
FRB20210309F	118.5, 6.5	–	547	S171	118.2, 5.4	–	1.39	WISE
FRB20200828D	118.9, 7.7	0.96 ± 0.96	1517	S171	118.2, 5.4	–	1.39	WISE
FRB20190912D	119.3, 3.9	–	786.2	S171	118.3, 4.9	0.84 ± 0.31	0.73	WISE
				S171	118.2, 5.4	–	1.39	WISE
FRB20220218A	120.1, 5.4	–	594.5	S171	118.2, 5.4	–	1.39	WISE
FRB20200806B	121.8, 0.8	–	2766	–	121.3, 0.7	–	–	HH14
FRB20220330A	124.9, 0.9	0.367 ± 0.37	664.9	–	125, 0.9	–	0.12	WISE
FRB20220814A	127.5, 1	0.919 ± 0.92	1431	–	127, 0.8	–	–	HH14
				–	127.6, 1.1	–	0.2	WISE
FRB20190302A	133.2, 0.2	11.28 ± 11	1034	S190; W3	133.5, 0.8	–	0.46	WISE
FRB20200416A	134.8, 1.2	0.702 ± 0.7	538.6	–	134.8, 0.9	–	–	HH14
				W4; S190	135.8, 0.9	–	0.69	WISE
				W4; S190	135, 0.7	3.31 ± 0.35	0.87	WISE
FRB20181014A	137.2, 4.2	0.478 ± 0.48	1314	–	138.1, 4.1	–	–	HH14
FRB20191231B	138, 3.9	–	703.2	–	138.1, 4.1	–	–	HH14

Table 2. Continued.

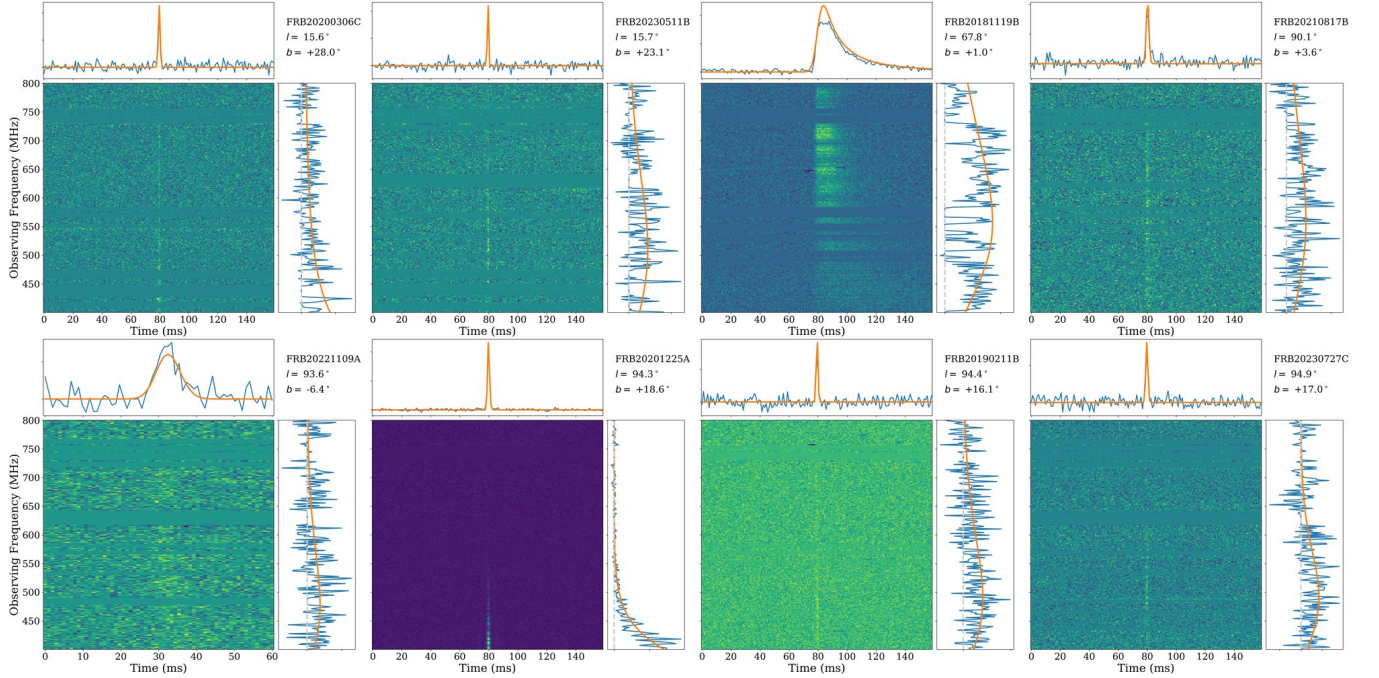
TNS Name	(l, b)	τ_{sc}	DM	Name	(l, b)	D	θ_{IR}	Catalog
	(deg)	(ms at 1 GHz)	(pc cm ⁻³)		(deg)	(kpc)	(deg)	
FRB20200708A	138.2, -1.1	7.998 ± 8	842.5	–	139.7, -1.2	–	1.52	WISE
FRB20230218B	138.3, 4.1	–	590.9	–	138.1, 4.1	–	–	HH14
FRB20191209B	138.9, 2.9	–	910.7	–	139.6, 2.5	3.81 ± 0.34	0.38	WISE
FRB20221129E	140.8, 2.7	1.709 ± 1.7	2293	–	141.7, 2.8	–	–	HH14
				–	140.8, 3.1	–	–	HH14
				–	140.8, 3.1	–	0.21	WISE
				–	140.6, 1.9	–	–	HH14
FRB20210512A	141.4, 4.5	0.345 ± 0.34	778.7	–	140.8, 3.1	–	–	HH14
FRB20190325C	142, 3.5	–	797.9	–	141.7, 2.8	–	–	HH14
				–	140.8, 3.1	–	–	HH14
FRB20210207E	142.6, 2	–	479	–	142.2, 2.1	–	–	HH14
				–	141.7, 2.8	–	–	HH14
				–	142.2, 2	–	0.43	WISE
FRB20211001B	143.5, -1	–	378.7	–	143.8, -1.6	–	–	HH14
				S203	143.6, -1.5	3.39 ± 0.25	0.36	WISE
FRB20230709B	146.6, 4.2	–	514.9	–	146.1, 3.1	–	0.69	WISE
FRB20200717B	150.7, 2.9	–	295.2	S207	151.2, 2.5	–	0.46	WISE
FRB20230418E	152.3, 2.6	0.592 ± 0.59	497.5	S210	152.7, 2.9	1.67 ± 0.34	0.31	WISE
FRB20210925B	152.8, -20.9	–	1027	–	158.1, -21.4	–	–	HH14
FRB20210813B	154.4, -20.9	–	518.4	–	158.3, -20.5	–	–	HH14
				–	158.1, -21.4	–	–	HH14
FRB20220518E	156, -17.8	–	377	–	158.3, -20.5	–	–	HH14
				–	158.1, -21.4	–	–	HH14
FRB20200112E	156.1, -0.6	–	913.7	–	155.4, -0.3	–	0.53	WISE
FRB20230730A	156.3, -19.7	–	312.6	–	158.3, -20.5	–	–	HH14
				–	158.1, -21.4	–	–	HH14
FRB20210920D	156.5, -20.5	0.618 ± 0.62	1201	–	158.3, -20.5	–	–	HH14
				–	158.1, -21.4	–	–	HH14
FRB20211013D	158.4, -17.6	–	1091	–	158.3, -20.5	–	–	HH14
				–	158.1, -21.4	–	–	HH14
FRB20220424A	158.5, -26.1	–	1373	–	158.1, -21.4	–	–	HH14
FRB20211231B	158.6, -11.9	–	905.7	–	160.5, -12.1	–	–	HH14
				California Nebula; S220	160, -12.7	0.77 ± 0.31	1.58	WISE
FRB20211120B	159, -18.7	–	359.1	–	158.3, -20.5	–	–	HH14
				–	158.1, -21.4	–	–	HH14
				–	159.9, -18.6	0.24 ± 0.02	0.78	WISE
FRB20221012E	159.1, -15.1	0.457 ± 0.46	1118	California Nebula; S220	160, -12.7	0.77 ± 0.31	1.58	WISE
FRB20220304A	159.3, -24.2	–	334.3	–	158.1, -21.4	–	–	HH14
				–	158.3, -20.5	–	–	HH14
FRB20210210A	159.6, -26.1	–	401.9	–	158.1, -21.4	–	–	HH14
FRB20201030C	159.7, -21.3	–	974.2	–	158.1, -21.4	–	–	HH14
				–	158.3, -20.5	–	–	HH14
FRB20201017C	159.7, -11.3	0.659 ± 0.66	731.9	–	160.5, -12.1	–	–	HH14
				California Nebula; S220	160, -12.7	0.77 ± 0.31	1.58	WISE
FRB20211116A	160.6, -25.4	–	775.1	–	158.1, -21.4	–	–	HH14

Table 2. Continued.

TNS Name	(l, b)	τ_{sc}	DM	Name	(l, b)	D	θ_{IR}	Catalog
	(deg)	(ms at 1 GHz)	(pc cm ⁻³)		(deg)	(kpc)	(deg)	
FRB20200323G	160.6, -9.7	0.212 ± 0.21	627.9	California Nebula; S220	160, -12.7	0.77 ± 0.31	1.58	WISE
FRB20191215C	161, -22	–	260.5	–	158.1, -21.4	–	–	HH14
				–	158.3, -20.5	–	–	HH14
FRB20230910C	162.6, -19.1	0.634 ± 0.63	660.1	–	158.1, -21.4	–	–	HH14
				–	158.3, -20.5	–	–	HH14
FRB20210507A	163.3, -8.4	–	525.8	–	165.4, -9	–	–	HH14
FRB20200131A	168.8, -21.1	–	1359	–	176.2, -20.9	–	–	HH14
FRB20230915E	169.6, -16.7	–	621.1	–	176.2, -20.9	–	–	HH14
FRB20220818B	170.7, -2	0.285 ± 0.28	1286	–	172, -2.2	–	–	HH14
FRB20210330D	171.3, -24.3	–	2280	–	176.2, -20.9	–	–	HH14
FRB20200626A	171.4, -3	–	1580	–	173, -1.3	–	–	HH14
				–	172, -2.2	–	–	HH14
FRB20220405A	172.2, -17.6	–	462.4	–	176.2, -20.9	–	–	HH14
				–	178.9, -20.1	–	–	HH14
FRB20220719F	172.4, -1	–	525.3	–	173, -1.3	–	–	HH14
				–	172, -2.2	–	–	HH14
FRB20221025I	173.9, -21.1	–	453.3	–	178.9, -20.1	–	–	HH14
				–	176.2, -20.9	–	–	HH14
FRB20190902B	173.9, 2.8	–	758.2	–	173.4, 2.4	–	–	HH14
				–	173.4, 2.6	–	–	HH14
				–	173.4, 3.2	–	–	HH14
				–	173.6, 2.8	–	–	HH14
				S235	173.5, 3.2	–	0.38	WISE
FRB20181119D	174.9, -0.1	–	566.4	–	173, -1.3	–	–	HH14
FRB20200929A	175.3, -16.2	–	821.4	–	178.9, -20.1	–	–	HH14
				–	176.2, -20.9	–	–	HH14
FRB20210111D	175.4, -25.7	–	890.8	–	178.9, -20.1	–	–	HH14
				–	176.2, -20.9	–	–	HH14
FRB20210412C	176.2, -16.6	–	463.9	–	178.9, -20.1	–	–	HH14
				–	176.2, -20.9	–	–	HH14
FRB20230725F	176.3, -18.5	–	838.4	–	178.9, -20.1	–	–	HH14
				–	176.2, -20.9	–	–	HH14
FRB20221218C	178.4, -16.1	–	372.1	–	176.2, -20.9	–	–	HH14
				–	178.9, -20.1	–	–	HH14
FRB20190418A	179.4, -22.9	–	184.5	–	176.2, -20.9	–	–	HH14
				–	178.9, -20.1	–	–	HH14
FRB20221223G	180.1, -22.1	–	618.8	–	176.2, -20.9	–	–	HH14
				–	178.9, -20.1	–	–	HH14
FRB20190712A	180.2, -32.5	–	682.5	–	186.3, -34.3	–	–	HH14
FRB20201026E	181.1, -20.8	–	804.8	–	176.2, -20.9	–	–	HH14
				–	178.9, -20.1	–	–	HH14
FRB20200412A	181.3, -18.3	–	839.5	–	176.2, -20.9	–	–	HH14
				–	178.9, -20.1	–	–	HH14
FRB20230717C	181.8, -18.1	0.473 ± 0.47	231.2	–	178.9, -20.1	–	–	HH14
				–	176.2, -20.9	–	–	HH14

Table 2. Continued.

TNS Name	(l, b)	τ_{sc}	DM	Name	(l, b)	D	θ_{IR}	Catalog
	(deg)	(ms at 1 GHz)	(pc cm ⁻³)		(deg)	(kpc)	(deg)	
FRB20230705E	183.2, -31	0.291 ± 0.29	596.1	–	186.3, -34.3	–	–	HH14
FRB20230106B	184.1, -24.3	–	595.7	–	178.9, -20.1	–	–	HH14
FRB20220710B	184.5, -34.8	–	190.7	–	186.3, -34.3	–	–	HH14
FRB20200922C	185, -29.6	–	498.2	–	186.3, -34.3	–	–	HH14
FRB20200119D	185.3, -24.4	–	944	–	178.9, -20.1	–	–	HH14
FRB20230730C	185.4, -19.4	–	227.2	–	178.9, -20.1	–	–	HH14
FRB20210327F	185.5, -29	0.293 ± 0.29	287.5	–	186.3, -34.3	–	–	HH14
FRB20190617B	186.2, -39.4	0.437 ± 0.44	272.6	–	186.3, -34.3	–	–	HH14
FRB20221021C	186.3, -19.8	–	721.6	–	178.9, -20.1	–	–	HH14
FRB20190103B	191.3, 1.1	1.008 ± 1	540.7	–	192.3, 0.8	–	0.6	WISE
FRB20210304E	192.3, -3.5	–	1144	–	192.2, -3.8	–	–	HH14
FRB20230615B	193.3, -14.7	–	608	–	194.6, -15.6	–	–	HH14
FRB20190427A	194.5, -17.1	–	455.9	–	194.6, -15.6	–	–	HH14
FRB20190409A	195.7, -17.2	–	1792	–	194.6, -15.6	–	–	HH14
FRB20230905D	196.8, -0.5	2.163 ± 2.2	443.7	S268	196.8, -2.4	–	1.06	WISE
FRB20191014B	196.9, -12.1	–	278.2	–	195.1, -12	–	–	HH14
				S264; lambda Ori	195.3, -12.1	–	0.84	WISE
FRB20211204B	217.2, 1.8	–	425.9	–	216.7, 1.1	–	0.64	WISE

B.2. Waterfall Plots**Figure 7.** Observed dynamic spectra (colorized maps), time-averaged spectra (right-hand panels), and band-averaged timeseries (top panels) for CHIME/FRB detections that intersect known H II regions as described in §5.2. The orange lines in the one-dimensional panels represent the best-fit shapes and spectral energy distributions determined by *fitburst*.

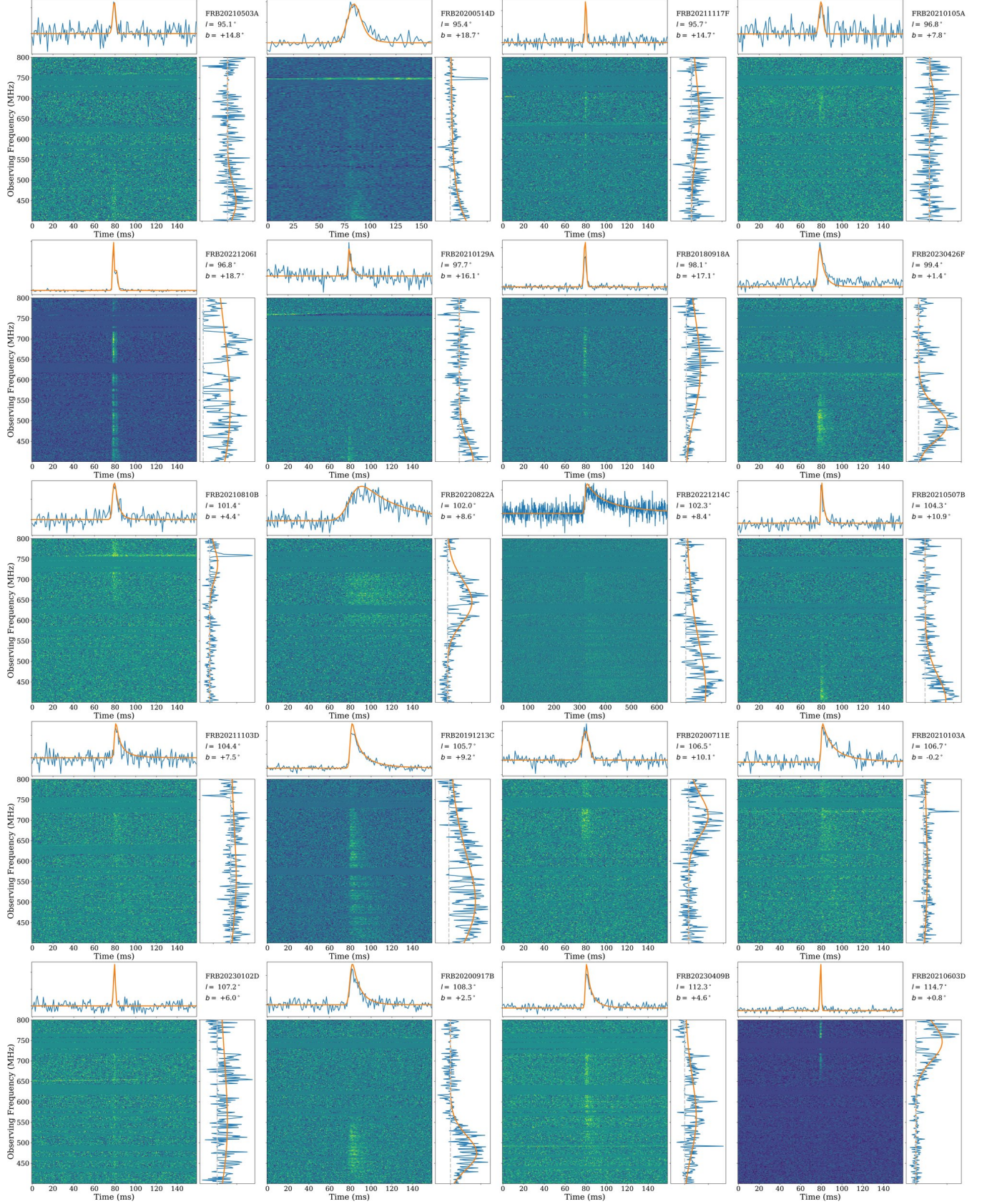


Figure 7. Continued.

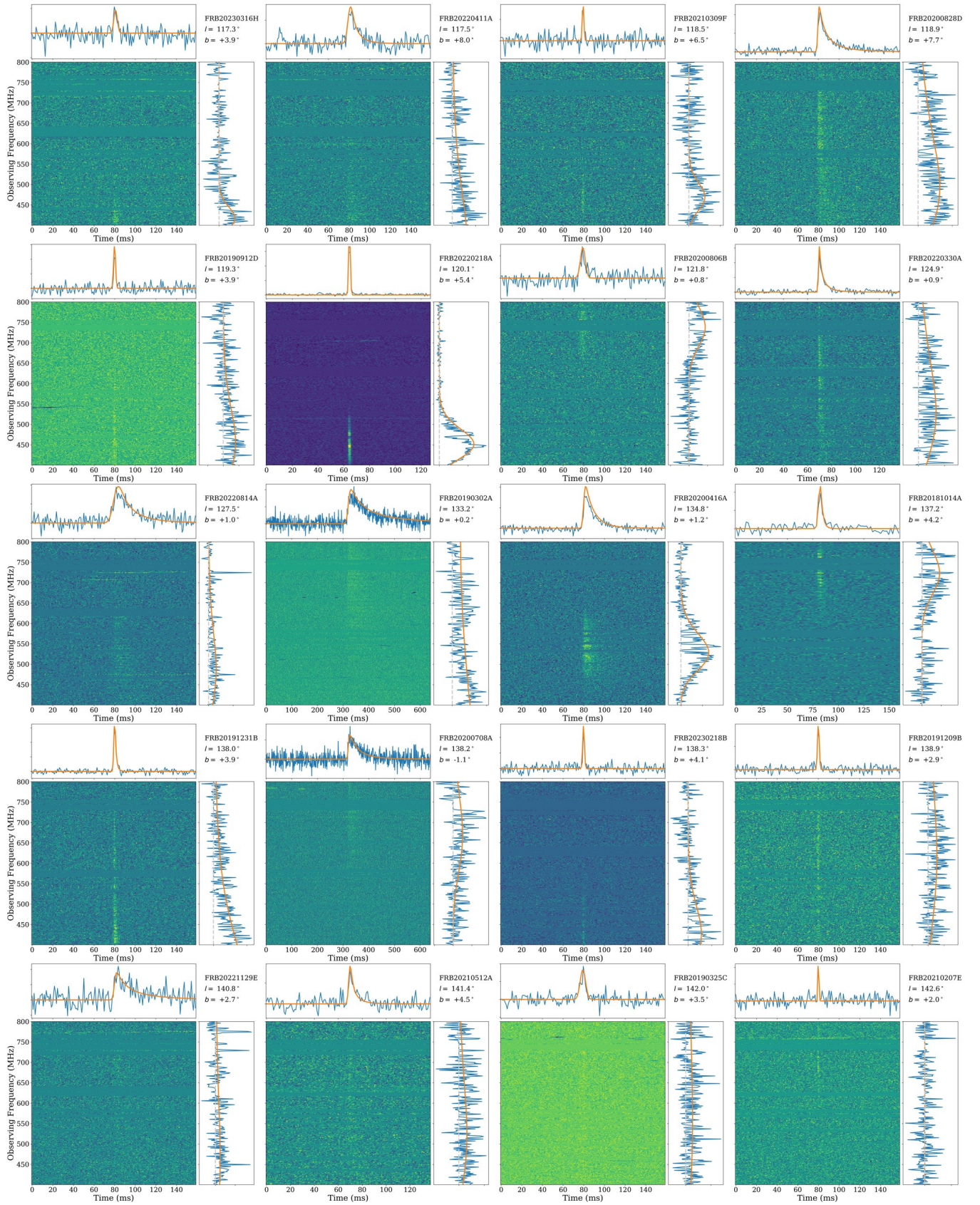


Figure 7. Continued.

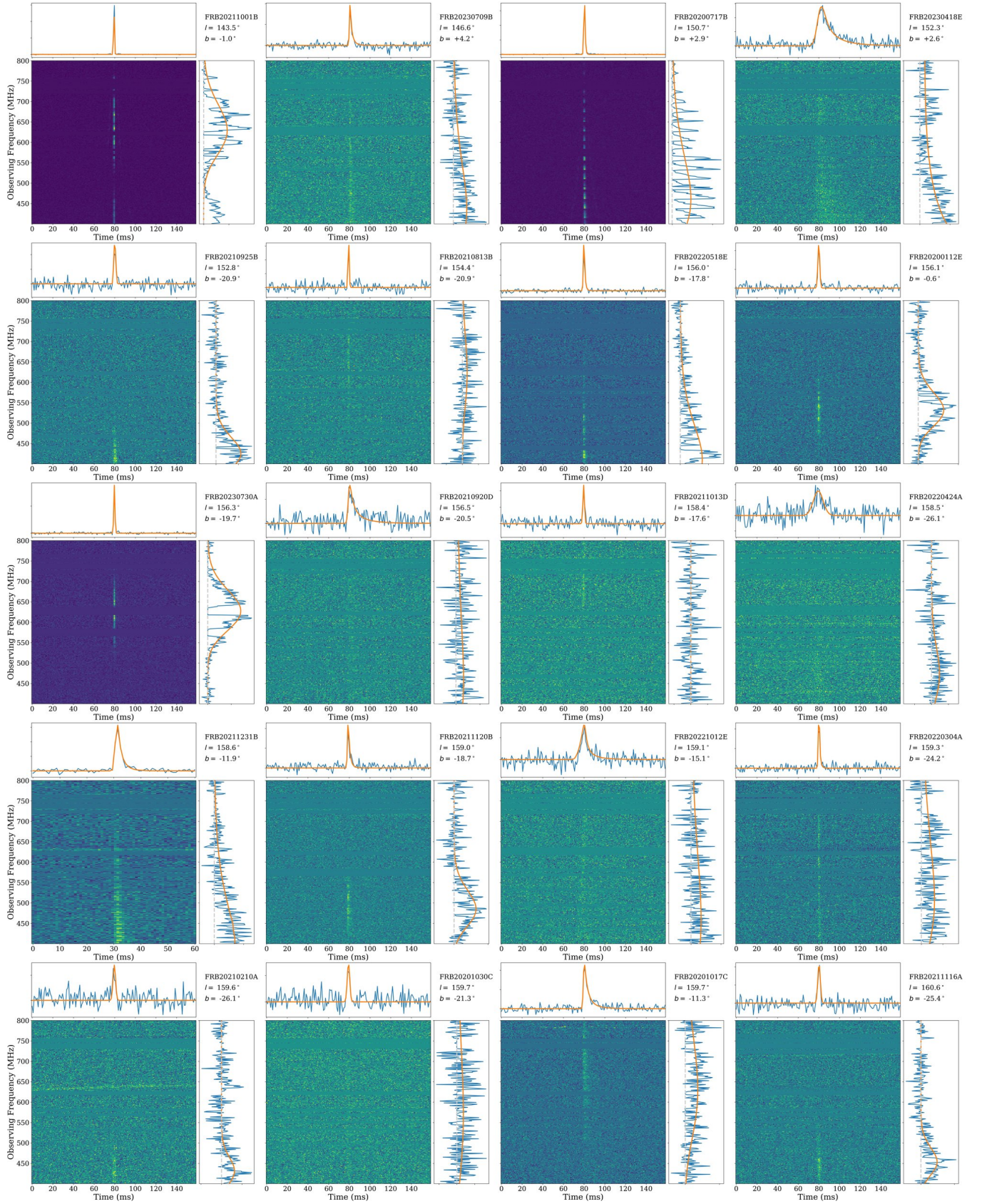


Figure 7. Continued.

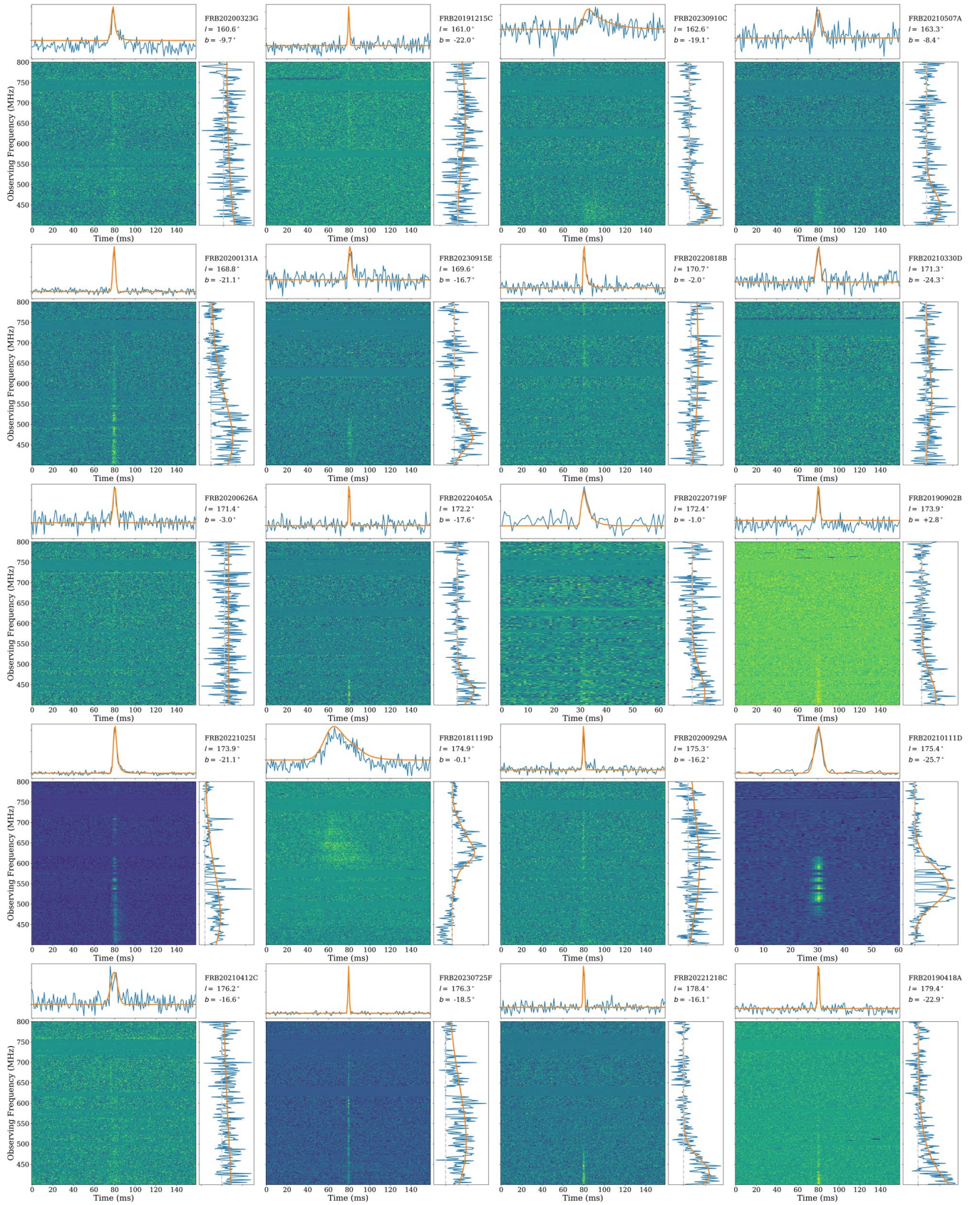


Figure 7. Continued.

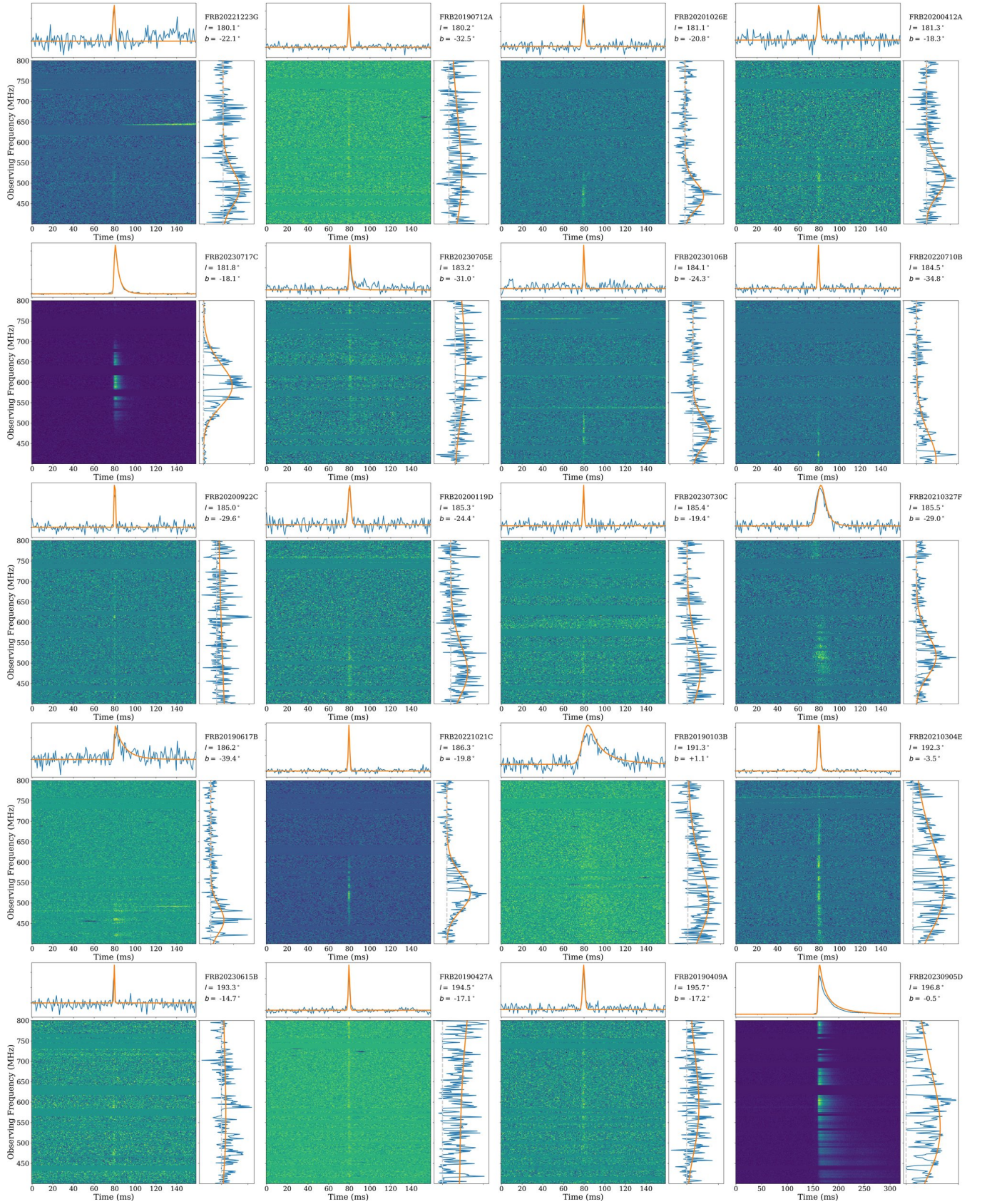


Figure 7. Continued.

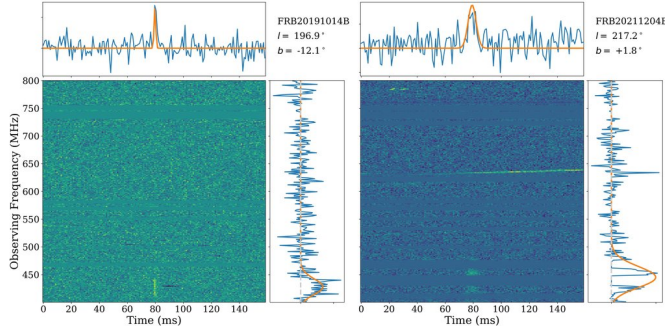


Figure 7. Continued.

C. REDUCED EXPOSURE

During part of the observing duration, there was reduced exposure between declinations $\sim 27^\circ$ and $\sim 34^\circ$ due to a period of computational downtime as shown in Figure 8. A dip in exposure is present in the area enclosed by gray square.

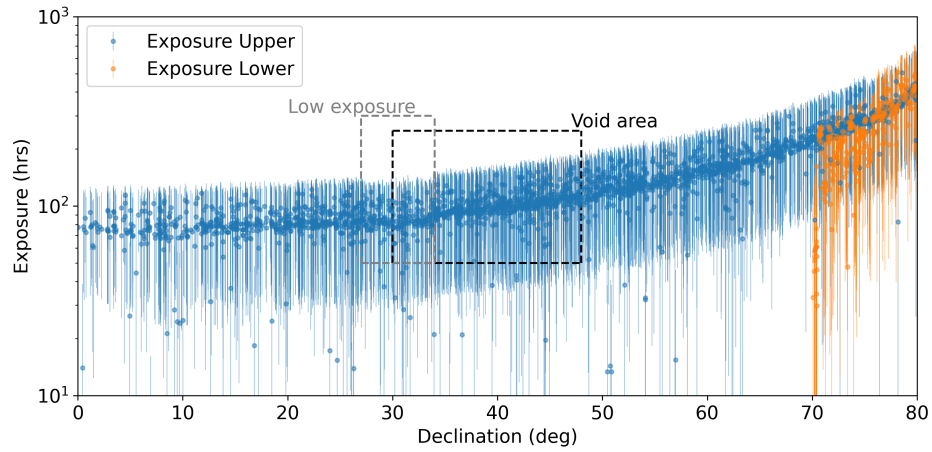


Figure 8. Exposure time (in hours) as a function of declination for both upper and lower transit beams. Low exposure region corresponding to a period of computational downtime is indicated by gray square and the detection gap area is highlighted by black square.

REFERENCES

- Anderson, L. D., Bania, T., Balser, D. S., et al. 2014, *The Astrophysical Journal Supplement Series*, 212, 1
- Anderson, L. D., Bania, T. M., Balser, D. S., et al. 2014, *ApJS*, 212, 1, doi: [10.1088/0067-0049/212/1/1](https://doi.org/10.1088/0067-0049/212/1/1)
- Berlanas, S. R., Wright, N. J., Herrero, A., Drew, J. E., & Lennon, D. J. 2019, *MNRAS*, 484, 1838, doi: [10.1093/mnras/stz117](https://doi.org/10.1093/mnras/stz117)
- Bhat, N. D. R., Cordes, J. M., Camilo, F., Nice, D. J., & Lorimer, D. R. 2004, *ApJ*, 605, 759, doi: [10.1086/382680](https://doi.org/10.1086/382680)
- Bochenek, C. D., Ravi, V., Belov, K. V., et al. 2020, *Nature*, 587, 59, doi: [10.1038/s41586-020-2872-x](https://doi.org/10.1038/s41586-020-2872-x)
- CHIME Collaboration, Amiri, M., Bandura, K., et al. 2022, *ApJS*, 261, 29, doi: [10.3847/1538-4365/ac6fd9](https://doi.org/10.3847/1538-4365/ac6fd9)
- CHIME/FRB Collaboration, Amiri, M., Bandura, K., et al. 2018, *ApJ*, 863, 48, doi: [10.3847/1538-4357/aad188](https://doi.org/10.3847/1538-4357/aad188)
- CHIME/FRB Collaboration, Andersen, B. C., Bandura, K., et al. 2019, *ApJL*, 885, L24, doi: [10.3847/2041-8213/ab4a80](https://doi.org/10.3847/2041-8213/ab4a80)
- CHIME/FRB Collaboration, Andersen, B. C., Bandura, K. M., et al. 2020, *Nature*, 587, 54, doi: [10.1038/s41586-020-2863-y](https://doi.org/10.1038/s41586-020-2863-y)
- CHIME/FRB Collaboration, Amiri, M., Andersen, B. C., et al. 2021, *ApJS*, 257, 59, doi: [10.3847/1538-4365/ac33ab](https://doi.org/10.3847/1538-4365/ac33ab)
- CHIME/FRB Collaboration, Amiri, M., Andersen, B. C., et al. 2025, arXiv e-prints, arXiv:2504.05192, doi: [10.48550/arXiv.2504.05192](https://doi.org/10.48550/arXiv.2504.05192)
- CHIME/FRB Collaboration et al. 2025, Submitted to *ApJS*
- CHIME/Pulsar Collaboration, Amiri, M., Bandura, K. M., et al. 2021, *ApJS*, 255, 5, doi: [10.3847/1538-4365/abfdcb](https://doi.org/10.3847/1538-4365/abfdcb)
- Comerón, F., Djupvik, A. A., Schneider, N., & Pasquali, A. 2020, *A&A*, 644, A62, doi: [10.1051/0004-6361/202039188](https://doi.org/10.1051/0004-6361/202039188)
- Cook, A. M., Bhardwaj, M., Gaensler, B. M., et al. 2023, *ApJ*, 946, 58, doi: [10.3847/1538-4357/acbbd0](https://doi.org/10.3847/1538-4357/acbbd0)
- Cook, A. M., Li, D., Eadie, G. M., et al. 2024, arXiv e-prints, arXiv:2410.12146, doi: [10.48550/arXiv.2410.12146](https://doi.org/10.48550/arXiv.2410.12146)
- Cordes, J., Wharton, R., Spitler, L., Chatterjee, S., & Wasserman, I. 2016, arXiv preprint arXiv:1605.05890
- Cordes, J. M., & Chatterjee, S. 2019, *ARA&A*, 57, 417, doi: [10.1146/annurev-astro-091918-104501](https://doi.org/10.1146/annurev-astro-091918-104501)
- Cordes, J. M., & Lazio, T. J. W. 2002, arXiv preprint astro-ph/0207156
- Cordes, J. M., & McLaughlin, M. A. 2003, *ApJ*, 596, 1142, doi: [10.1086/378231](https://doi.org/10.1086/378231)
- Cordes, J. M., Wharton, R. S., Spitler, L. G., Chatterjee, S., & Wasserman, I. 2016, arXiv e-prints, arXiv:1605.05890, doi: [10.48550/arXiv.1605.05890](https://doi.org/10.48550/arXiv.1605.05890)
- Curtin, A. P., Sand, K. R., Pleunis, Z., et al. 2024, arXiv e-prints, arXiv:2411.02870, doi: [10.48550/arXiv.2411.02870](https://doi.org/10.48550/arXiv.2411.02870)
- Desai, K. M., & Fey, A. L. 2001, *ApJS*, 133, 395, doi: [10.1086/320349](https://doi.org/10.1086/320349)
- Dey, J., Pandian, J. D., Lal, D. V., et al. 2024, *A&A*, 689, A254, doi: [10.1051/0004-6361/202450043](https://doi.org/10.1051/0004-6361/202450043)
- Emig, K. L., White, G. J., Salas, P., et al. 2022, *A&A*, 664, A88, doi: [10.1051/0004-6361/202142596](https://doi.org/10.1051/0004-6361/202142596)
- Fey, A. L., Spangler, S. R., & Cordes, J. M. 1991, *ApJ*, 372, 132, doi: [10.1086/169960](https://doi.org/10.1086/169960)
- Fey, A. L., Spangler, S. R., & Mutel, R. L. 1989, *ApJ*, 337, 730, doi: [10.1086/167144](https://doi.org/10.1086/167144)
- Finkbeiner, D. P. 2003, *ApJS*, 146, 407, doi: [10.1086/374411](https://doi.org/10.1086/374411)
- Fonseca, E., Pleunis, Z., Breitman, D., et al. 2024, *ApJS*, 271, 49, doi: [10.3847/1538-4365/ad27d6](https://doi.org/10.3847/1538-4365/ad27d6)
- Gabányi, K. É., Krichbaum, T. P., Britzen, S., et al. 2006, *A&A*, 451, 85, doi: [10.1051/0004-6361:20054017](https://doi.org/10.1051/0004-6361:20054017)
- Gardenier, D. W., Connor, L., van Leeuwen, J., Oostrum, L. C., & Petroff, E. 2021, *A&A*, 647, A30, doi: [10.1051/0004-6361/202039626](https://doi.org/10.1051/0004-6361/202039626)
- Hallinan, G., Ravi, V., Weinreb, S., et al. 2019, in *Bulletin of the American Astronomical Society*, Vol. 51, 255, doi: [10.48550/arXiv.1907.07648](https://doi.org/10.48550/arXiv.1907.07648)
- Han, J. L., Zhou, D. J., Wang, C., et al. 2025, *Research in Astronomy and Astrophysics*, 25, 014001, doi: [10.1088/1674-4527/ada3b7](https://doi.org/10.1088/1674-4527/ada3b7)
- Haslam, C. G. T., Salter, C. J., Stoffel, H., & Wilson, W. E. 1982, *A&AS*, 47, 1
- Hou, L. G., & Han, J. L. 2014a, *VizieR Online Data Catalog: Spiral structure of the Milky Way (Hou+, 2014)*, VizieR On-line Data Catalog: J/A+A/569/A125. Originally published in: 2014A&A...569A.125H doi: [10.26093/cds/vizier.35690125](https://doi.org/10.26093/cds/vizier.35690125)
- Hou, L. G., & Han, J. L. 2014b, *A&A*, 569, A125, doi: [10.1051/0004-6361/201424039](https://doi.org/10.1051/0004-6361/201424039)
- Jing, W. C., Han, J. L., Wang, C., et al. 2025, arXiv e-prints, arXiv:2506.14519, doi: [10.48550/arXiv.2506.14519](https://doi.org/10.48550/arXiv.2506.14519)
- Joseph, A., Chawla, P., Curtin, A. P., et al. 2021, *ApJ*, 923, 2, doi: [10.3847/1538-4357/ac33ad](https://doi.org/10.3847/1538-4357/ac33ad)
- Koay, J. Y., Jauncey, D. L., Hovatta, T., et al. 2019, 489, 5365, doi: [10.1093/mnras/stz2488](https://doi.org/10.1093/mnras/stz2488)
- Koryukova, T. A., Pushkarev, A. B., Kiehlmann, S., & Readhead, A. C. S. 2023, *MNRAS*, 526, 5932, doi: [10.1093/mnras/stad3052](https://doi.org/10.1093/mnras/stad3052)
- Krishnarao, D., Benjamin, R. A., & Haffner, L. M. 2020, *ApJL*, 899, L11, doi: [10.3847/2041-8213/aba8f0](https://doi.org/10.3847/2041-8213/aba8f0)
- Lazio, T. J. W., & Fey, A. L. 2001, *ApJ*, 560, 698, doi: [10.1086/322958](https://doi.org/10.1086/322958)
- Lin, H.-H., Scholz, P., Ng, C., et al. 2024, *ApJ*, 975, 75, doi: [10.3847/1538-4357/ad779d](https://doi.org/10.3847/1538-4357/ad779d)
- Lorimer, D. R., Bailes, M., McLaughlin, M. A., Narkevic, D. J., & Crawford, F. 2007, *Science*, 318, 777, <https://arxiv.org/abs/0709.4301>
- Luisi, M., Anderson, L. D., Liu, B., Anish Rosh, D., & Churchwell, E. 2019, *ApJS*, 241, 2, doi: [10.3847/1538-4365/aaf6a5](https://doi.org/10.3847/1538-4365/aaf6a5)

- Macquart, J.-P., & Johnston, S. 2015, *MNRAS*, 451, 3278, doi: [10.1093/mnras/stv1184](https://doi.org/10.1093/mnras/stv1184)
- Mall, G., Main, R. A., Antoniadis, J., et al. 2022, *MNRAS*, 511, 1104, doi: [10.1093/mnras/stac096](https://doi.org/10.1093/mnras/stac096)
- Manchester, R. N., Hobbs, G. B., Teoh, A., & Hobbs, M. 2005, *AJ*, 129, 1993, doi: [10.1086/428488](https://doi.org/10.1086/428488)
- McEwen, A. E., Lynch, R. S., Kaplan, D. L., et al. 2024, *ApJ*, 969, 118, doi: [10.3847/1538-4357/ad47f0](https://doi.org/10.3847/1538-4357/ad47f0)
- McKinnon, M. M. 2014, *PASP*, 126, 476, doi: [10.1086/676975](https://doi.org/10.1086/676975)
- McKinnen, R., Gaensler, B. M., Michilli, D., et al. 2023a, *ApJ*, 950, 12, doi: [10.3847/1538-4357/acc65f](https://doi.org/10.3847/1538-4357/acc65f)
- McKinnen, R., Gaensler, B. M., Michilli, D., et al. 2023b, *ApJ*, 951, 82, doi: [10.3847/1538-4357/acd188](https://doi.org/10.3847/1538-4357/acd188)
- McKinnen, R., Bhardwaj, M., Eftekhari, T., et al. 2025, *Nature*, 637, 43, doi: [10.48550/arXiv.2402.09304](https://doi.org/10.48550/arXiv.2402.09304)
- Merryfield, M., Tendulkar, S. P., Shin, K., et al. 2023, *AJ*, 165, 152, doi: [10.3847/1538-3881/ac9ab5](https://doi.org/10.3847/1538-3881/ac9ab5)
- Mezger, P. G., & Henderson, A. P. 1967, *ApJ*, 147, 471, doi: [10.1086/149030](https://doi.org/10.1086/149030)
- Mezger, P. O. 1978, *A&A*, 70, 565
- Michilli, D., Masui, K. W., McKinnen, R., et al. 2021, *ApJ*, 910, 147, doi: [10.3847/1538-4357/abe626](https://doi.org/10.3847/1538-4357/abe626)
- Molnar, L. A., Mutel, R. L., Reid, M. J., & Johnston, K. J. 1995, *ApJ*, 438, 708, doi: [10.1086/175115](https://doi.org/10.1086/175115)
- Morgan, J. S., Chhetri, R., & Ekers, R. 2022, *PASA*, 39, e063, doi: [10.1017/pasa.2022.56](https://doi.org/10.1017/pasa.2022.56)
- Nimmo, K., Pleunis, Z., Beniamini, P., et al. 2025, *Nature*, 637, 48, doi: [10.1038/s41586-024-08297-w](https://doi.org/10.1038/s41586-024-08297-w)
- Ocker, S. K., Anderson, L. D., Lazio, T. J. W., Cordes, J. M., & Ravi, V. 2024, *ApJ*, 974, 10, doi: [10.3847/1538-4357/ad6a51](https://doi.org/10.3847/1538-4357/ad6a51)
- Ocker, S. K., Cordes, J. M., Chatterjee, S., & Gorsuch, M. R. 2022, *ApJ*, 934, 71, doi: [10.3847/1538-4357/ac75ba](https://doi.org/10.3847/1538-4357/ac75ba)
- Pandhi, A., Pleunis, Z., McKinnen, R., et al. 2024, *ApJ*, 968, 50, doi: [10.3847/1538-4357/ad40aa](https://doi.org/10.3847/1538-4357/ad40aa)
- Patel, C., Agarwal, D., Bhardwaj, M., et al. 2018, *ApJ*, 869, 181, doi: [10.3847/1538-4357/aaee65](https://doi.org/10.3847/1538-4357/aaee65)
- Petroff, E., Hessels, J. W. T., & Lorimer, D. R. 2022, *A&A Rv*, 30, 2, doi: [10.1007/s00159-022-00139-w](https://doi.org/10.1007/s00159-022-00139-w)
- Piddington, J. H., & Minnett, H. C. 1952a, *Australian Journal of Scientific Research A Physical Sciences*, 5, 17, doi: [10.1071/CH9520017](https://doi.org/10.1071/CH9520017)
- Piddington, J. H., & Minnett, H. C. 1952b, *Australian Journal of Scientific Research A Physical Sciences*, 5, 17, doi: [10.1071/CH9520017](https://doi.org/10.1071/CH9520017)
- Planck Collaboration, Adam, R., Ade, P. A. R., et al. 2016, *A&A*, 594, A10, doi: [10.1051/0004-6361/201525967](https://doi.org/10.1051/0004-6361/201525967)
- Platts, E., Weltman, A., Walters, A., et al. 2019, *PhR*, 821, 1, doi: [10.1016/j.physrep.2019.06.003](https://doi.org/10.1016/j.physrep.2019.06.003)
- Quireza, C., Rood, R. T., Bania, T. M., Balser, D. S., & Maciel, W. J. 2006, *ApJ*, 653, 1226, doi: [10.1086/508803](https://doi.org/10.1086/508803)
- Ravi, V., Catha, M., Chen, G., et al. 2025, *AJ*, 169, 330, doi: [10.3847/1538-3881/adc725](https://doi.org/10.3847/1538-3881/adc725)
- Rygl, K. L. J., Brunthaler, A., Sanna, A., et al. 2012, *A&A*, 539, A79, doi: [10.1051/0004-6361/201118211](https://doi.org/10.1051/0004-6361/201118211)
- Sand, K. R., Curtin, A. P., Michilli, D., et al. 2024, arXiv e-prints, arXiv:2408.13215, doi: [10.48550/arXiv.2408.13215](https://doi.org/10.48550/arXiv.2408.13215)
- Sand, K. R., Curtin, A. P., Michilli, D., et al. 2025, *ApJ*, 979, 160, doi: [10.3847/1538-4357/ad9b11](https://doi.org/10.3847/1538-4357/ad9b11)
- Schneider, N., Bontemps, S., Simon, R., et al. 2006, *A&A*, 458, 855, doi: [10.1051/0004-6361:20065088](https://doi.org/10.1051/0004-6361:20065088)
- Shin, K., Leung, C., Simha, S., et al. 2024, arXiv e-prints, arXiv:2410.07307, doi: [10.48550/arXiv.2410.07307](https://doi.org/10.48550/arXiv.2410.07307)
- Su, M., Slatyer, T. R., & Finkbeiner, D. P. 2010, *ApJ*, 724, 1044, doi: [10.1088/0004-637X/724/2/1044](https://doi.org/10.1088/0004-637X/724/2/1044)
- The CHAMPSS Collaboration, Andrade, C., Boyle, P. J., et al. 2025, arXiv e-prints, arXiv:2504.16293, doi: [10.48550/arXiv.2504.16293](https://doi.org/10.48550/arXiv.2504.16293)
- Thornton, D., Stappers, B., Bailes, M., et al. 2013, *Science*, 341, 53. <https://arxiv.org/abs/1307.1628>
- Vanderlinde, K., Liu, A., Gaensler, B., et al. 2019, in *Canadian Long Range Plan for Astronomy and Astrophysics White Papers*, Vol. 2020, 28, doi: [10.5281/zenodo.3765414](https://doi.org/10.5281/zenodo.3765414)
- Virtanen, P., Gommers, R., Oliphant, T. E., et al. 2020, *Nature Methods*, 17, 261, doi: [10.1038/s41592-019-0686-2](https://doi.org/10.1038/s41592-019-0686-2)
- Walker, M. A., Melrose, D. B., Stinebring, D. R., & Zhang, C. M. 2004, *MNRAS*, 354, 43, doi: [10.1111/j.1365-2966.2004.08159.x](https://doi.org/10.1111/j.1365-2966.2004.08159.x)
- Wendker, H. J., Higgs, L. A., & Landecker, T. L. 1991, *A&A*, 241, 551
- Williamson, I. P. 1972, *MNRAS*, 157, 55, doi: [10.1093/mnras/157.1.55](https://doi.org/10.1093/mnras/157.1.55)
- Wucknitz, O. 2012, in *Proceedings of the 11th European VLBI Network Symposium & Users Meeting*. 9-12 October, 49, doi: [10.22323/1.178.0049](https://doi.org/10.22323/1.178.0049)
- Wucknitz, O. 2014, in *Proceedings of the 12th European VLBI Network Symposium and Users Meeting (EVN 2014)*. 7-10 October 2014. Cagliari, ed. A. Tarchi, M. Giroletti, & L. Feretti, 66, doi: [10.22323/1.230.0066](https://doi.org/10.22323/1.230.0066)
- Xu, J., Feng, Y., Li, D., et al. 2023, *Universe*, 9, 330, doi: [10.3390/universe9070330](https://doi.org/10.3390/universe9070330)
- Yao, J. M., Manchester, R. N., & Wang, N. 2017, *ApJ*, 835, 29, doi: [10.3847/1538-4357/835/1/29](https://doi.org/10.3847/1538-4357/835/1/29)
- Zhou, D. J., Han, J. L., Zhang, B., et al. 2022, *Research in Astronomy and Astrophysics*, 22, 124001, doi: [10.1088/1674-4527/ac98f8](https://doi.org/10.1088/1674-4527/ac98f8)
- Zhou, D. J., Han, J. L., Jing, W. C., et al. 2023, *MNRAS*, 526, 2657, doi: [10.1093/mnras/stad2769](https://doi.org/10.1093/mnras/stad2769)